Eindhoven University of Technology

MASTER

All-solution processed regular organic solar cells using a new inkjet-printable cathode

van Franeker, J.J.

Award date:
2012

Link to publication

Disclaimer
This document contains a student thesis (bachelor's or master's), as authored by a student at Eindhoven University of Technology. Student theses are made available in the TU/e repository upon obtaining the required degree. The grade received is not published on the document as presented in the repository. The required complexity or quality of research of student theses may vary by program, and the required minimum study period may vary in duration.

General rights
Copyright and moral rights for the publications made accessible in the public portal are retained by the authors and/or other copyright owners and it is a condition of accessing publications that users recognise and abide by the legal requirements associated with these rights.

- Users may download and print one copy of any publication from the public portal for the purpose of private study or research.
- You may not further distribute the material or use it for any profit-making activity or commercial gain

ALL-SOLUTION PROCESSED REGULAR ORGANIC SOLAR CELLS USING A NEW INKJET-PRINTABLE CATHODE

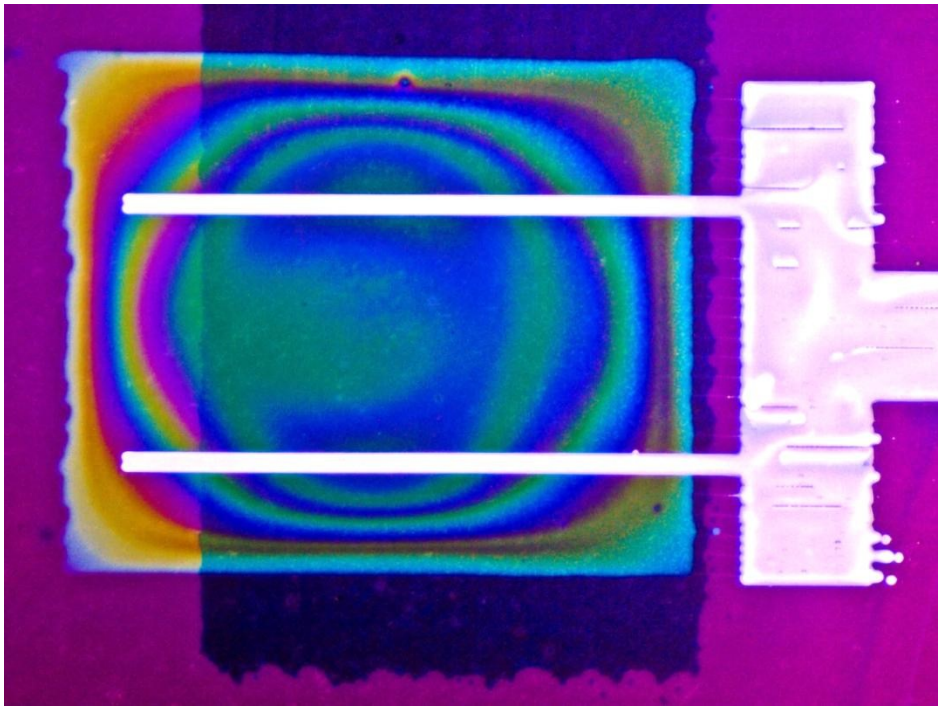

Author:	**J.J. van Franeker** (0671360)
Graduation project report for:	**Sustainable Energy Technology**
Supervision by:	**dr. Yulia Galagan** (Holst Centre)
	prof. dr. ir. R.A.J. Janssen (TU/e department of Chemical Engineering and Chemistry, group Molecular Materials and Nanosystems)
Final presentation and defense:	**14:00** in **STO4.91** on **28 June 2012**

ABSTRACT

The current developments in polymer organic solar cells are inspired by the idea that they can be processed entirely from solution. In all polymer cells the photoactive layer is processed from solution, most often the electrodes are not. Holst Centre has already developed a solution-processable anode, this project focusses on the development of a solution-processable cathode[1] for solar cells with a "regular" configuration – that is, the cathode has to be processed on top of the other layers.

To make a solution-processable cathode it is required to use high-workfunction metals which can be processed in the form of ink, like silver. When silver is used a cathode modification layer (Electron Transport Layer or ETL) is required. Out of several of materials for these layers that have been studied two were successful: zinc oxide (ZnO) processed from a nanoparticle dispersion in acetone and the polymer PFN which has been dissolved in ethanol. Solar cells with these ETLs and an evaporated silver cathode perform 12% lower than the reference design (with a LiF aluminum cathode). When comparing the reference design with an evaporated silver electrode without ETL the performance loss is 43%, thus the ETL significantly improves performance.

The printing of silver on top of the ZnO layer was problematic because of crack formation. It was however shown that the principle worked, thus several methods were employed to prevent cracks. None gave reliable results. The layers were studied using AFM, conductive AFM, SEM and cross-sectional TEM. The printing of silver on top of PFN was successful: 35 out of 40 produced cells were working with the best performances reaching over 50% of the performance of the reference design. This success warranted the combination of the Holst anode with the new cathode to create all-solution processed devices with photovoltaic power conversion efficiencies reaching 1.95%.

[1] In solar cells the term cathode can be subject to multiple definitions. In this thesis the term cathode is used for the contact where electrons are injected into the device under forward bias larger than the open-circuit voltage. Then subsequently the anode is the contact where holes are injected into the device under the same conditions.

CONTENTS

1 INTRODUCTION

The currently record high gasoline price leads to economic uncertainty and civil unrest. The cause - the high crude oil price - is not expected to decrease soon. The high oil price is caused both by political instability in the Middle East and by the depletion of many sources ('peak oil') [1–3]. The best alternatives for transportation fuels are based on electrical power. Currently our electricity is generated in large part by coal powered power plants. Apart from the associated air pollution and global warming the working conditions of coal miners are highly risky [4,5]. To decrease this dependency on such polluting, scarce and uncertain resources it is very important to look for alternatives among which solar energy is a promising candidate. The sun provides as much energy in one hour as the amount of energy that is used by the whole planet in one year [6].

The photovoltaic effect was discovered by Becquerel in 1839 [7]. Then, in 1941 Russel Ohl from Bell Laboratories discovered the silicon 'p-n junction' solar cells [8]. The efficiency has been increasing and the costs have been decreasing due to the upscaling of production. Currently the European solar cell manufacturers are pushed out of the market by Chinese companies that are able to sell at even lower prices. The solar cell market has been growing with 30% a year [9], but the price of solar energy is still higher than the price of "coal" energy in Northern Europe. Various strategies are employed to further reduce costs of which one is the development of organic solar cells.

Organic solar cells are based on organic materials instead of silicon. These materials can be processed in a solution under ambient conditions and thus layered structures can be formed by conventional printing and coating methods. This promise would enable the production of vast areas of solar cells on plastic foil by roll-to-roll processes (see Figure 1).

Figure 1 – Holst Centre roll-to-roll line

There have been a few reports of "All Solution Processed" (ASP) organic solar cells. However, most often the electrodes are not processed by solution-based methods – the used process being expensive and not roll-to-roll compatible. The most common practice in research today is the use of expensive ITO (Indium-Tin-Oxide, thus containing the scarce material Indium) coated glass plates on which a few organic layers are deposited by solution. Then the other electrode is deposited on top by physical vapor deposition (PVD) which requires a vacuum chamber. Often aluminum is used which also requires handling in an inert atmosphere, because aluminum is highly reactive with oxygen. There are some reports either replacing the ITO [10,11] or the evaporated electrode [12,13] by a solution-compatible process. A report of an all-solution processed solar cell was presented at E-MRS in May 2011 [14] and there are also reports of all-solution processed but laminated devices [15].

At Holst Centre work has focused on the development of solution-processable electrodes. The layer of the solar cells that actually captures the sunlight (the photoactive layer or PAL) is under investigation at other research institutes. For this project the PAL always consists of the same, commonly used combination of P3HT[2] and PCBM[2] [16]. At Holst Centre the ITO anode has been replaced by silver grids, covered with high-conducting PEDOT:PSS[2] [17–19]. Silver can be deposited by solution processing in air using printing and coating methods [19–21].

To replace the evaporated cathode by a solution-processable cathode also the aluminum has to be replaced by silver. The different properties of this metal require an additional "inter"layer between the PAL and the silver. It is known that for example Zinc Oxide (ZnO) [12,22] can be used as such an interlayer and hence ZnO will be the

[2] Full names are given in experimental sections (chapter 3)

starting point for this project. The transition from evaporated metals to solution processed silver however is not straightforward. This project will focus on the development of efficient, roll-to-roll compatible and reproducible methods to produce a solution processed cathode.

2 THEORY AND CHARACTERIZATION

This section starts with a general overview of the operation principle of organic solar cells (OSC). This overview then focusses on the parts which are most important in this project: charge extraction at the cathode. Then a large section is devoted to the characterization of organic solar cells, most notably *J-V* curves. This is important when trying to understand the interplay of effects involved in the charge extraction at the cathode. The last section uses this theoretical framework to explain the possibilities and problems encountered in the development of a solution processable cathode.

2.1 OPERATION PRINCIPLE

A general overview is given regarding the operation of organic solar cells. The aim is not to be complete but to give insight in the relevant processes required to understand the effect of the interlayer and cathode materials on the device parameters.

2.1-I ORGANIC PHOTOVOLTAICS: DONOR AND ACCEPTOR

When a photon is absorbed in the active area of an organic solar cell it promotes an electron in a molecule to an excited state. This state is called an exciton. This excited state and the corresponding energy can move around the polymer chains a little bit – this "exciton diffusion length" is in the range of 5-8 nm in P3HT [24]. To obtain an electrical current from a solar cell the energy of this exciton needs to be converted into electric charges that can move larger distances: an electron and the corresponding 'empty spot': a hole. It was found by Tang [25] that this conversion happens very efficiently at an interface between two organic materials which have been called "donor" and "acceptor". The donor polymer (P3HT) "donates" an electron to the acceptor fullerene (PCBM) and a hole stays behind. This process is called exciton disassociation by charge transfer. After dissociating, the electrons and holes move apart by both drift and diffusion which are both important for device operation [26]. The electron transfers through the acceptor to the cathode while the hole transfers through the donor to the anode.

2.1-II BULK HETEROJUNCTION

It was soon realized that the diffusion length of the exciton limits the efficiency of the organic solar cells. If the interface between donor and acceptor cannot be reached within the exciton lifetime the energy will be lost. Thus each exciton should be able to reach a donor-acceptor interface within the exciton diffusion length (which is 5-8 nm). Hence there should ideally be such an interface "everywhere" in the device. Sariciftci and Heeger [27] came with a solution for this problem in the form of a bulk heterojunction (BHJ, Figure 2) where donor and acceptor are intimately mixed on the nanometer scale.

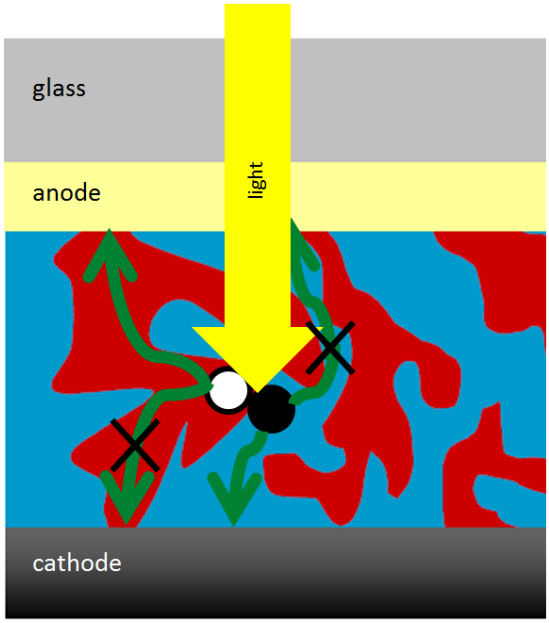

Figure 2 - BHJ structure with indicated processes: green arrows indicate possible electron and hole extraction, however the crossed processes should not happen [23]

2.1-III CHARGE EXTRACTION

In a BHJ there is an additional problem because both donor and acceptor are connected to both electrodes. Electrons and holes can go either way (green arrows in Figure 2). To generate current the holes need to go in one direction (to the anode) and the electrons in the other (to the cathode). This problem is solved when electrodes are made selective for either electrons or holes, thereby effectively blocking the charges going in the "wrong" direction. This can be done by aligning the energy level of the anode with the energy of the hole in the donor (the highest occupied molecular orbital or HOMO level) and aligning the energy level of the cathode with the energy of the hole in the acceptor (the lowest unoccupied molecular orbital or LUMO). Band bending (see section 2.3-I) then blocks the undesired charge extraction.

A common device architecture for organic solar cells (e.g. [30]) is shown in Figure 3. This architecture or "stack" is used as reference in this project. Holes are extracted at the ITO | PEDOT:PSS anode and electrons are extracted at the Lithium Fluoride | Aluminum (LiF|Al) cathode which is prepared by vapor deposition. The thin (~1 nm) layer of LiF is inserted to lower the workfunction of aluminum [29,31,32].

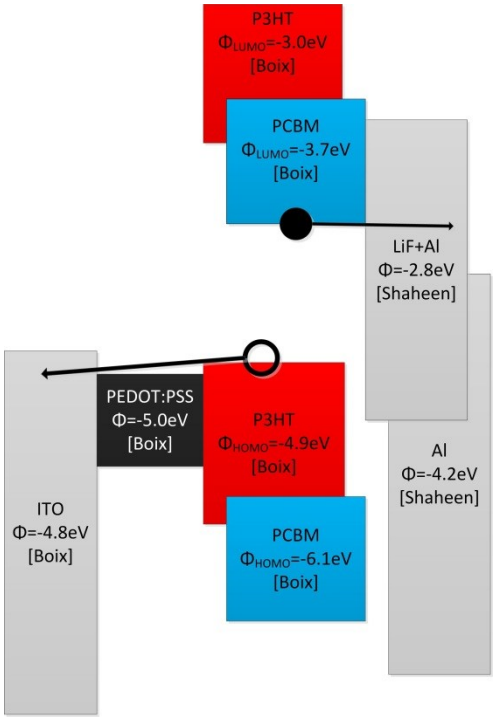

Figure 3 – Energy Level Diagram of "reference" design. Sources: Boix: [28] **Shaheen:** [29]

2.2 CHARACTERIZATION

Usually the first and most important characterization of solar cells is a measurement under simulated sunlight. This will be described in section 2.2-I. Methods to analyze these graphs are introduced in section 2.2-II. To gain insight in the wetting behavior of various liquids on various organic layers it is useful to perform contact angle measurements to determine surface properties. Because no results from these measurements are given this section is included as Appendix 6.1.

2.2-I *J-V* CURVES

A common method to characterize organic solar cells is to measure the current density (*J*) through the solar cell at different bias voltages (*V*). This can be done either under simulated solar irradiation or in the dark. Such data can be plotted in a *J-V* curve, a typical example is shown in Figure 4.

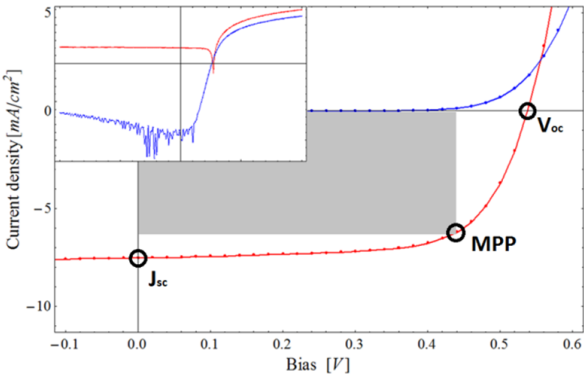

Figure 4 - Typical *J-V* curve for an organic solar cell (inset: logarithmic plot)

2.2-I A) PARAMETERS: J_{SC}, V_{OC}, FF, MPP

Four parameters can be directly determined from the *J-V* curve under simulated sunlight. The short circuit current density (J_{sc}) is the current density at zero voltage bias. The open circuit voltage (V_{oc}) is the voltage at which the current is zero. The maximum power point is the point on the curve where the generated power (MPP = $J_{mpp} * V_{mpp}$) is maximal. Finally, the fill factor (FF) is defined by $\mathrm{FF} = {\mathrm{MPP}}/{J_{sc} * V_{oc}}$.

The short circuit current density is determined by the number of absorbed photons and the collection efficiency. There is still debate in literature to explain the origin of the open circuit voltage – it is related to the HOMO-LUMO difference of respectively the donor and acceptor – but a more extensive overview is given in section 2.3-I. The fill factor is related to how easily charges can be extracted and is influenced by the "series" and "shunt" resistance which will be defined in section 2.2-II.

2.2-I B) SHAPE

The shape of a *J-V* curve contains a large amount of information. The parameters listed in the previous section are most often used to characterize the solar cell, but they are far from complete. For example, as illustrated in Figure 5, a decrease in fill factor could have two possible causes:

1. The increase in current density for increasing voltage is less steep (curved red line).
2. The current density in the negative direction bias is not constant but bias-dependent (straight red line).

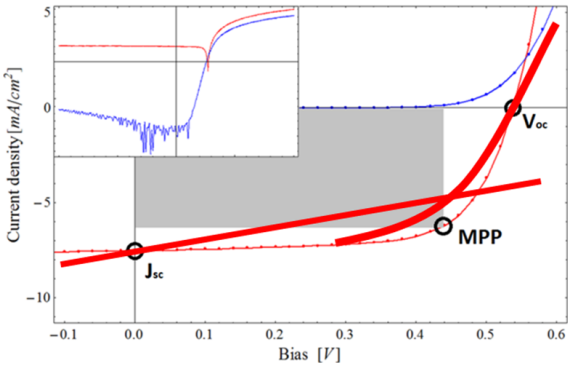

Figure 5 – Decrease of fill factor by different cause

From the fill factor only it is not possible to know what was the cause, even though the physical origin is obviously different. For example, cause 1 could originate from a contact problem or bad electrodes, while cause 2 could originate from a shunt that cannot be neglected or problems with the extraction of charges.

An even more pronounced effect appears when there is an unexpected energy barrier. The standard 'J-shaped' *J-V* curve can than transform into an 'S-shaped' form in which an inflection point appears (see Figure 6). This is related to a problem with the extraction and injection of charge carriers, as explained by Lilliedal et al [33] and numerically simulated by Wagenpfahl et al [34]. The model assumes a limited surface recombination velocity which causes a build-up of space charge, that in turn causes the current to be space-charge limited (SCLC) and show the characteristic S-shape. In this project a S-shape is often related to the absorption of oxygen on the ZnO and can be resolved by a UV-treatment [32,33,35–37].

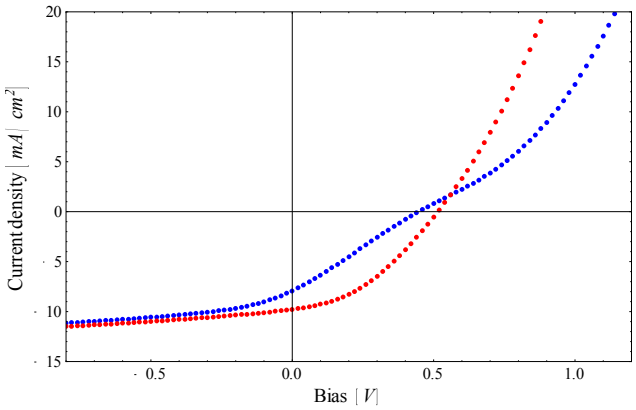

Figure 6 – S-shaped *J-V* curve (blue) and after 10 minutes UV-treatment (red)

The aim of this section is to show that just the reporting of the 'standard' device parameters is not enough for a complete description of the current-voltage characteristics. To use a numerical description more parameters are needed. These will be introduced in section 2.2-II. To obtain these parameters it was convenient to introduce a database system, which will be explained in the next section.

2.2-I C) DATABASE

Large amounts of *J-V* curves were measured. It was desired to analyze some parameters for all these measurements and this could be done more conveniently with a database system which is described here.

A researcher in the field of organic solar cells manufactures several solar cells on a typical lab day. After a couple of months a large amount of *J-V* data obtained from different solar cell stacks is available. The trained scientist can extract valuable information from the *J-V* curve by visually analyzing the plot, for example about parasitic currents or contact problems. This is often done while still in the lab or shortly after – the data is most often not saved using a systematic and convenient method for further use.

In most measurement setups the 'raw' data is saved as a textual file. Then typical desktop software can be used to plot the *J-V* curve again. This plotting however is a work-intensive process. Therefore this is often only done for graphs that are to be included in either a paper, report or presentation. A large amount of the collected data is never used again.

These large amounts of unused data have potential uses. Statistical methods can be employed to gain insight in the reproducibility and perhaps in factors involved in the variation of performance from one day to another or from one researcher to another. It would also allow researchers involved in modeling to use large amount of experimental data to check their models.

A more systematic way to store the obtained *J-V* data is a database system. For this purpose I designed the database setup shown in Figure 7. The raw *J-V* data is stored in a table ('JV') – one row for each measurement. Each cell has certain properties which are listed in a separate table 'JVpars'. Then each device has a structure which is coupled in the table 'devices'. More devices can have the same structure so all structures are listed in a separate table ('structures'). Structures consist of different 'layers'.

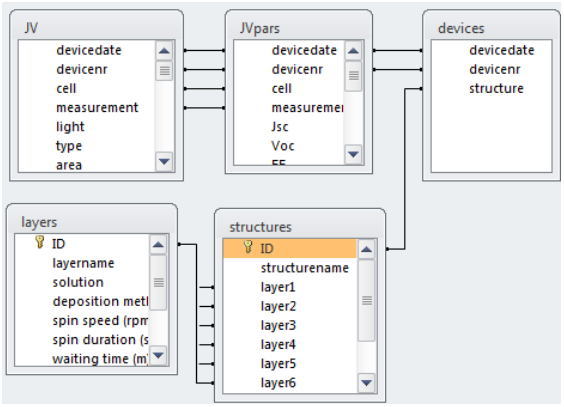

Figure 7 - Database structure and relationships

This database has been set up using Microsoft Access 2010. This database software does not allow for convenient plotting and analysis of the *J-V* data. For this purpose a coupling is possible with Wolfram Mathematica 8.0 which is a mathematical software package. To implement the database structure several module sections had to be written in Mathematica code. The fundamental sequence is as follows:

1. Automated import of *J-V* data from textual files to database
2. The code asks the user for the structure of all new devices (it is also possible to add new layers and structures)
3. To proceed all *J-V* curves have to be checked for incomplete measurements and shorts – this is done by showing all new measurements and asking the user to give this information
4. Then all correct measurements are automatically analyzed using the procedures described in the sections below
5. Finally all extracted data is shown in a list – here it is possible to select certain measurements for plotting or to statistically analyze the extracted data – see appendix 6.2 for a screenshot of the user interface.

The setup of this database system allows the user to compare data very efficiently. A wide implementation of an improved version of this system could ease the use of data, which has advantages for both the individual and the research group:

1. For the individual researcher: saves time and allows for the more regular comparison of data, which could indicate systematic problems and lead to new insights, as shown by Riede et al [38].
2. For the research group: Improve collaboration between researchers and allow modeling to be done on large amounts of data. Allows the comparison of reference devices and results between researchers.

Currently at the research institute IMEC (Leuven) an online database (SoloDB) is used to keep track of the fabrication of the solar cells. Also an automated setup is used to measure all cells on one devices in a sequence. The combination of such systems with the database described above could result in more efficient lab use due to planning tools and quicker measuring which would save expensive lab-time and increase the pace of innovation.

2.2-II PARAMETER EXTRACTION

Inorganic solar cells are often characterized by a single diode model of which the equivalent circuit diagram is shown in Figure 8. This model has also been used for organic solar cells [30,40–42], but it is also known that is not physically correct [39,43]. Organic solar cells for example have bimolecular recombination mechanisms and the bulk-heterojunction structure can cause undesired recombination at the contacts. An example of the deviation from the diode model is shown in Figure 9: the slope in reverse bias is different in the dark than under simulated sunlight conditions. This cannot be explained by the (constant) shunt resistance and bias-independent photocurrent in the diode model and shows that the solar cell parameters will depend on the illumination level.

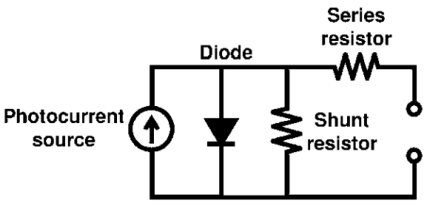

Figure 8 – Single diode model (taken from [39])

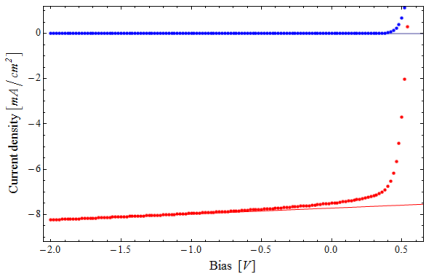

Figure 9 - Reverse bias current of reference OSC in the dark (blue) and under simulated sunlight conditions (red)

It can still be useful to assign numerical values to a *J-V* curve that describe the shape of the curve, to be able to compare different cells numerically, without having to visually inspect the *J-V* curves. The single diode model can be mathematically described by:

$$\text{(I)} \qquad J = J_0 \left[e^{\frac{q(V - J R_S)}{n k_b T}} - 1 \right] + \frac{V - J R_s}{R_{sh}} - J_{ph}$$

In this equation J_0 is the reverse bias saturation current density, q the electron charge, R_s the series resistance, R_{sh} the shunt resistance, n the diode ideality factor, k_b Boltzmann's constant and T the temperature. J_{ph} is the photocurrent which is assumed to be constant.

It is not possible to explicitly solve this transcendental equation for either *J* or *V* in terms of basic mathematical functions. Because of this a large variety of methods has been developed to extract the unknown device parameters from experimental *J-V* data.

2.2-II A) EASY METHOD: SLOPES

For an Ohmic resistance the relationship between current, voltage and resistance is given by the linear relationship $V = J\,R$. This means the slope of a *J-V* curve for an Ohmic device is related to the inverse of the resistance: $\frac{dJ}{dV} = \frac{1}{R}$. Of course an organic solar cell is not an Ohmic device. However, the single diode model includes two Ohmic resistances combined with a diode and a photocurrent.

Using equation (I) and neglecting the series resistance the only non-constant current at $V \sim 0$ flows through the shunt resistance. Thus, the shunt resistance (*slopeRsh*) can be estimated from

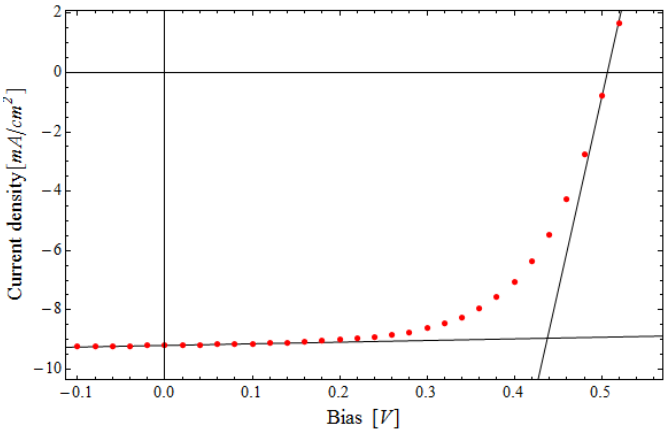

Figure 10 – Calculation of shunt and "*slopeVoc*" resistance using the inverse slope at V=0 and V=V_{oc}

the inverse slope of the *J-V* curve at zero bias.

The series resistance is related to the slope of the *J-V* curve at high bias voltage [30]. The *slope2V* is estimated as the average slope between 1.5V and 2V. However, according to Kim et al [44] it can also be approximated by the slope where $V \sim V_{oc}$. This is not correct when considering equation (I), because $J \sim 0$ in that regime – then R_s even falls out of the equation. However, the approach in [44] was still useful, because it was found that the slope around V_{oc} (*slopeVoc*) is fairly constant across devices with the same structure, but differs when comparing devices with a different structure and efficiency. It does serve a purpose of describing the form of the important region in the *J-V* curve with a number that can be analyzed using statistical methods.

2.2-II B) Fitting method – dark current

Two approaches have been employed to fit the diode equation. The first method uses *J-V* data obtained in the dark and will be discussed in this section. The second method uses *J-V* data obtained under simulated sunlight conditions and will be discussed in the next section.

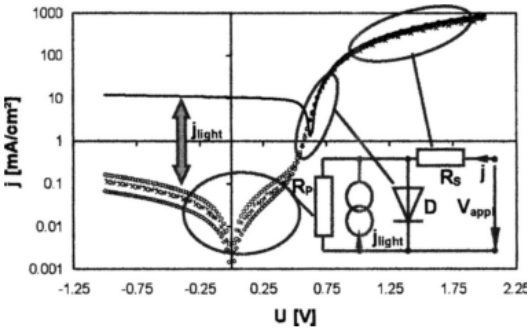

Figure 11 - Regimes in diode model (image taken from [30])

Using the measured dark current density the diode parameters are obtained according to the method of Lee et al [40]. The shunt resistance is estimated as *slopeRsh* (section 2.2-II A) Then, using equation (I) and assuming $R_s \sim 0$:

$$J \sim J_0 \left(\exp\left(\frac{q\,V}{n\,k\,T}\right) - 1\right) + \frac{V}{R_{shunt}} \rightarrow J + J_0 - \frac{V}{R_{shunt}} \sim J_0 \exp\left(\frac{q\,V}{n\,k\,T}\right) \rightarrow \ln\left(J + J_0 - \frac{V}{R_{shunt}}\right) \sim \ln(J_0) + \frac{q\,V}{n\,k\,T}$$

In the exponential regime, where the current is dominated by the diode parameters, the current is much larger than the dark saturation current density: $J \gg J_0$. Then we can plot $\ln(J_{measured} - V/R_{shunt})$ against *V*. This should give a straight line. Then J_0 can be determined from the intercept with the y-axis and *n* can be determined from the slope.

Now all parameters are known, except R_s. The series resistance is determined by fitting equation (I) to the experimental data using the FindFit function in Wolfram Mathematica 8.0. This whole process is iterated to obtain a better fit.

This fitting method gave unreliable results. Sometimes an accurate fit could be obtained but often the procedure did not converge or could not reproduce the experimental data. It was also observed (see Figure 9) that the diode parameters depended on the light intensity. For a solar cell the most relevant parameters are related to the performance under simulated sunlight thus this method was not used.

2.2-II C) Fitting method – light current

The *J-V* curve under simulated sunlight conditions can be described by the diode model using a set of five different parameters: J_{ph}, J_0, R_s, R_{sh} and *n*. It was shown by Zhang et al [45] that the amount of fitting parameters can be reduced to three by using the known parameters J_{sc} and V_{oc}. This method will be followed in this section.

The method employs the Lambert W function [46] which is defined so that it solves the equation $We^W = z$. The solution always has multiple "branches" of (complex) solutions which are implemented in mathematical software

like Wolfram Mathmetica (as the 'Productlog' function). Of these "branches" of solutions only the "principle branch" is necessary to be able to transform the diode equation [47] and obtain an equation for *J* as an explicit function of *V* [45]:

$$\text{(II)} \qquad J = \frac{V}{R_s} - \frac{R_{sh}\left(R_s J_{ph} + R_s J_0 + V\right)}{R_s(R_s + R_{sh})} + \frac{nk_bT}{qR_s} W\left[\frac{qR_s J_0 R_{sh}}{(R_s + R_{sh})nk_bT} exp\left(\frac{R_{sh}q(R_s J_{ph} + R_s J_0 + V)}{nk_bT(R_s + R_{sh})}\right)\right]$$

This equation could be used to fit to experimental data. However, this often leads to inconsistencies because of the large difference in magnitude between J_{ph} and J_0. This was solved by the use of equation (I) at both J=0 and V=0, for which the solution known through the parameters J_{sc} and V_{oc}:

$$\text{(III)} \qquad @V{=}0 \rightarrow J = -J_{sc} = J_0\left[e^{\frac{q\,J_{sc}\,R_s}{n\,k_b\,T}} - 1\right] + \frac{J_{sc}\,R_s}{R_{sh}} - J_{ph}$$

$$\text{(IV)} \qquad @V{=}V_{OC} \rightarrow J = 0 = J_0\left[e^{\frac{q\,V_{oc}}{n\,k_b\,T}} - 1\right] + \frac{V_{oc}}{R_{sh}} - J_{ph}$$

These two equations have five unknown parameters (J_{ph}, J_0, R_s, R_{sh} and n). It is thus possible to extract two - in our case J_0 and J_{ph} + J_0 - as a function of the other three and the known parameters J_{sc} and V_{oc}. These can then be substituted into equation (II), which gives a (long) equation for J in terms of only R_s, R_{sh} and n as unknown parameters. The full equation is listed in reference [45] of which the simplified version is used in this project. To fit the obtained equation to experimental data it is necessary to have an initial "guess" value for the three parameters. These are also obtained as listed in the reference. This fitting procedure gives consistent results and is thus mainly used in this project.

2.2-II D) Drift-diffusion device models

The diode equation is not entirely physically correct, as has been mentioned before. However, it does serve the purpose of describing the form of the *J-V* curve. A physically more realistic model involves solving the drift-diffusion equations as a function of the electric field. The purpose of this section is to list some of the parameters which are involved in these models. The potential distribution as a function of location in the device depends for example on the thickness, the injection barriers, the charge carrier concentration and the applied bias voltage and can be calculated using Poisson's equation. Then the current is calculated using the continuity equation, which depends on the potential distribution, the charge carrier density and both the electron and hole drift (given by mobilities μ) and electron and hole diffusion (given by diffusion constant D) [43]. This is still not the whole story, for example a limited surface recombination velocity could explain S-shaped *J-V* curves [34,48]. Also the shape of the density of states (DOS) and trap densities can be included to account for nongeminate recombination [49,50]. These models are not explicitly used in this project, but the results showing the effect of the involved parameters are kept in mind to be able to explain experimental results.

2.3 THE CATHODE

The goal of this project is to develop an all solution processable cathode. To be able to do this, it is important to understand the effects of the cathode on solar cell parameters. The described effects mainly concern the open circuit voltage and the reverse bias current, which in turn influences the fill factor and thus device performance. However, also the series resistance and thereby also the fill factor are influenced.

2.3-I OPEN-CIRCUIT VOLTAGE

The origin of the open circuit voltage in organic solar cells is a heavily debated subject. Many scientists are familiar with inorganic solar cells, where the V_{oc} is, amongst others, limited by the built-in potential caused by the doping of semiconductors. For organic solar cells the story is more difficult. As shown by Gregg and Hanna [26] the limit on V_{oc} in organic solar cells is not determined only by the built-in potential caused by the difference in workfunction between the electrodes but also by the chemical potential: after the excitons are separated there is a large concentration gradient away from the interface, which causes the charges to diffuse away from this interface to the collection electrodes. Organic solar cells thus depend not only on drift forces, but also diffusion.

Scharber et al [51] found a strong linear relationship between V_{oc} and the difference between HOMO energy level of the donor and the LUMO energy level of the acceptor (the energy "gap"). They found the empirical relationship for the open-circuit voltage:

$$V_{oc} = \frac{1}{e}\left[E_{HOMO}^{donor} - E_{LUMO}^{acceptor}\right] - 0.3V = E_{gap} - 0.3V \quad \text{(V)}$$

In which *e* is the elementary charge. The open-circuit voltage is strongly related to the onset voltage when the solar cell is operated as a diode in the dark. Kemerink *et al.* [52] argue that the onset voltage is when there are flat-band conditions in the bulk of the device – if the voltage is increased just a bit more drift and diffusion will go in the same direction and thus large currents can exist. The simplest possible band diagram for this situation is shown in Figure 12. They however indicate that there will be band bending which decreases the onset voltage (and thus the V_{oc}) – band bending is caused by the fact that the cathode has a high amount of free electrons while the PAL does not. Diffusion will thus cause electrons to move into the PAL, which will equilibrate the quasi Fermi levels [53] for electrons (the same will happen for holes at the anode) as is indicated in Figure 13. This band bending will have two effects:

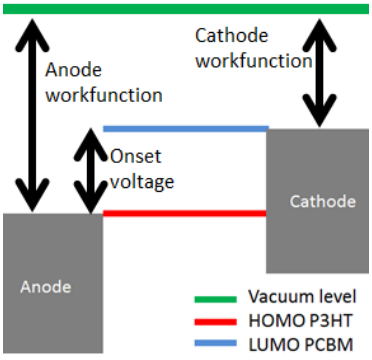

Figure 12 - Simplest band diagram at onset voltage. Injection barriers are not shown.

- The onset voltage is lowered, because flat-band conditions in the bulk happen at a lower voltage (imagine for example straight bands near the cathode in Figure 13c: the potential of electrode 2 will have to be higher to achieve flat bands).
- The bended bands form a barrier for 'the other' charge carriers: holes cannot be extracted at the cathode anymore, because they would have to overcome the bended bands. The same is true for electrons at the anode. Hence the electrodes have become selective.

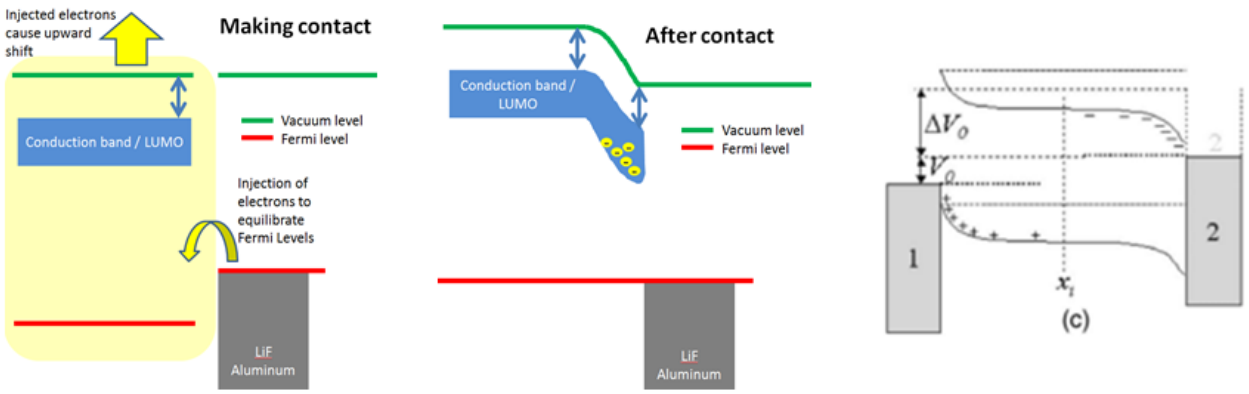

Figure 13 - When making contact electrons will be injected into the PAL to equilibrate quasi Fermi levels (left picture). This will cause band bending (middle picture). The band bending causes the onset voltage V_0 to decrease (picture (c), taken from [52])

The same principle is explained by Blakesley and Neher [54]: when operating at V_{oc} the current generated by the incident light is exactly matched by the recombination current in the opposite direction and thus no net current is generated. This means the quasi Fermi potentials for both electrons and holes will be constant and aligned with the contact workfunctions. When this balance between recombination and generation is modeled – assuming the Boltzmann approximation for carrier densities and bimolecular recombination - this leads to the empirical found reduction in V_{oc} with respect to the energy gap (equation (V)). They also argue that the standard energy-level picture is simplified. Disorder causes the existence of tail states in the energy gap. Ohmic contacts are defined as contacts which have their Fermi level aligned with the respective HOMO or LUMO level it should contact. When a metal is brought into Ohmic contact with a disordered polymer the tail states will be populated. It is proposed that these will cause the band-bending which results in the reduction of the open-circuit voltage [52,55]. There is thus an intimate relation between band-bending and disorder.

The previous paragraph thus assumed Ohmic contacts. However, if the contacts are not Ohmic they will have an important influence on the V_{oc}. An overview of the effects of the cathode workfunction is given by Mihailetchi [55]. It is shown that by varying the metal workfunction the V_{oc} can be varied over more than 0.5 V. It appears that the V_{oc} is either limited by the HOMO-LUMO gap or by the difference in contact workfunction. Mihailetchi observed that V_{oc} decreased when changing the cathode from LiF|Al to silver. He attributed this to the formation of a non-Ohmic contact due to the lower workfunction of silver and postulates the following equation:

$$\text{(VI)} \qquad V_{oc} = \frac{1}{e}\left[E_{HOMO}^{donor} - E_{LUMO}^{acceptor} - e\Delta V_b - \varphi_b\right]$$

For both anode and cathode there are two possible options: Ohmic or non-Ohmic. In the case of an Ohmic contact there will be band bending, reducing the voltage by ΔV_b. In the case of non-Ohmic contacts there will be an injection barrier φ_b which in turn decreases V_{oc}.

These explanations are intimately related to the concept of energy level alignment as explained by Ishii et al [56]. When an organic layer and a metal are brought into contact the Fermi levels will align, either by charge transfer - which causes band bending as introduced above - or by dipole formation due to rearrangements in the electron clouds. As explained in Figure 14, dipoles cause the vacuum energy levels to shift and can thus affect the energy gap – in the figure, the vacuum level on the right of the dipole is reduced and thus the LUMO of the organic material has a better alignment with the metal Fermi level than without a dipole.

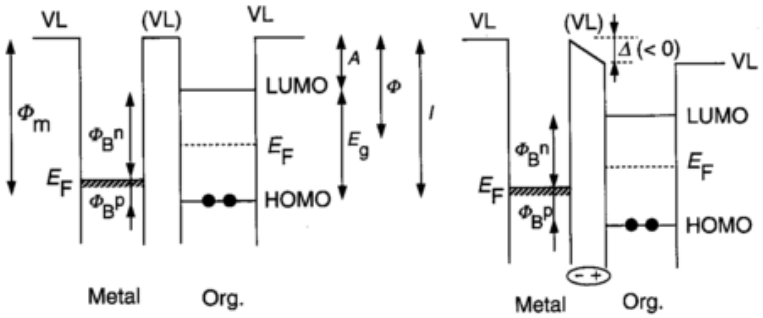

Figure 14 - Energy level shift caused by dipole formation (image taken from [56])

A more detailed insight is given with the integer charge transfer (ICT) model [57], where three regimes are identified: either the Fermi level is pinned to the positive or negative ICT-state by charge transfer with a corresponding shift in vacuum levels or - if the metal Fermi level is in between the positive and negative ICT-state – the vacuum levels will align. It is interesting to note that this Fermi-level pinning behavior is also observed in the model of Blakesley and Neher [54] described above. This behavior possibly relates to the observed effect of metal workfunction by Mihailetchi [55]. Low cathode workfunctions will align to the ICT- level by band bending, which means that from a certain limit even lower workfunction metals will make no difference: the energy level will be pinned to the ICT- level anyway. Higher metal workfunctions - which fall in between the two ICT levels - will not align and thus flat band conditions will happen at lower voltages. This is schematically indicated in Figure 13. Sehati *et al.* [57] indeed propose the ICT levels to be more relevant to the V_{oc} than just the HOMO/LUMO levels but do not claim this to be the complete story – the measured energy levels do not explain the measured V_{oc}'s which could be caused by the fact that the ICT levels are related to the most strongly bound charge pairs at the interface, which by itself do not contribute to the current.

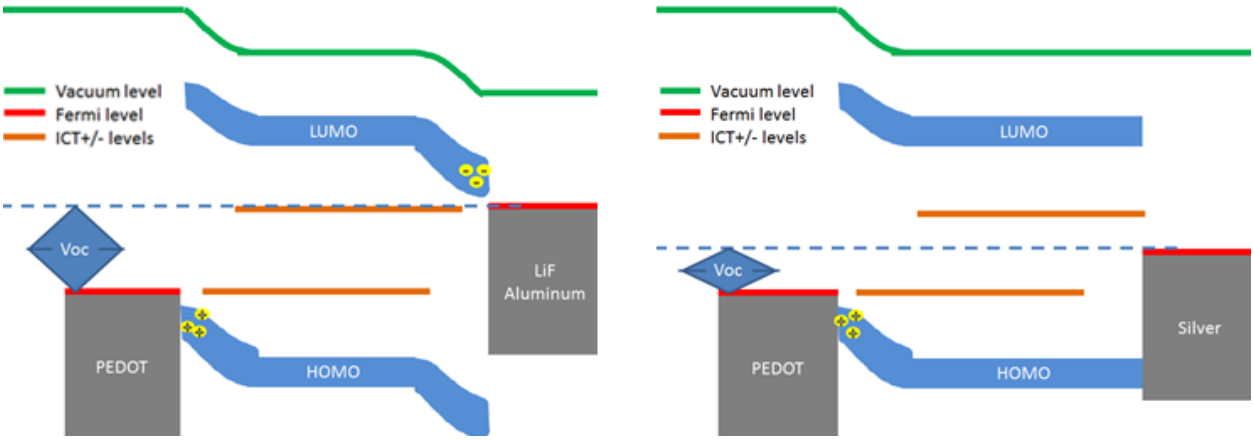

Figure 15 - Schematical indication of the effects of pinning to ICT levels

This section showed that the open-circuit voltage can depend on multiple factors related to the cathode: injection barriers, band bending, disorder and interfacial dipole formation. These all have to be kept in mind when determining suitable cathode materials.

2.3-II Electron Transporting Layer

When operating a solar cell the electrons should be extracted at the cathode. The free electrons in the LUMO level of the acceptor should be able to transfer into the cathode. This is facilitated by the alignment of the LUMO level with the workfunction of the cathode. If the cathode metal is not suitable for this purpose it is beneficial to insert an interlayer which facilitates the electron transport [22,28,32,40]: the Electron Transport Layer (ETL). The insertion of such a layer should decrease the series resistance, because it is easier for current to flow into the device in forward bias.

2.3-III Hole Blocking Layer

Holes should only be extracted at the anode. If holes are also extracted or if they recombine at the cathode the performance will decrease, because charges are lost. It will also show up in the reverse bias current in the dark. In forward bias holes enter the device through the anode, thus current is going from anode to cathode. In reverse bias, the current will be reversed thus will flow from cathode to anode, which means holes must enter the device from the cathode (or electrons from the anode, but we are interested in the cathode). It is desired to minimize the reverse bias current, thus the transport of holes from the cathode into the device should be limited. When the cathode metal is not suitable to prevent this it will be beneficial to insert a Hole Blocking Layer (HBL) to minimize the reverse bias current [28,32,40,58].

2.4 TOWARDS ALL SOLUTION PROCESSABLE CATHODE

At Holst Centre work has already been done to towards a solution processable anode [17,18] which consists of a silver grid with high-conducting PEDOT:PSS. The goal of this project is to develop an all-solution processable cathode.

In the "*reference*" device (Table 1) the cathode consists of Lithium Fluoride (1 nm) and Aluminum (100 nm) (LiF|Al). The inherent problem with the low workfunction of aluminum is the stability regarding oxidation. Therefore it is desired to use higher workfunction metals like silver (in the *onlyAg* design, Table 2), which can also be solution processed in the form of silver nanoparticle or silver complex inks. However, if the LiF|Al cathode is just replaced by an evaporated silver cathode the fill factor and open-circuit voltage decrease dramatically which causes a large decrease in efficiency.

Table 1 - "*Reference*" device architecture

Aluminum
LiF
P3HT / PCBM
PEDOT:PSS
ITO

Table 2 - "*onlyAg*" device architecture

Silver
P3HT / PCBM
PEDOT:PSS
ITO

Table 3 - "*ETL*" device architecture

Silver
ETL
P3HT / PCBM
PEDOT:PSS
ITO

2.4-I ETL

A possible solution to this problem is the insertion of both an electron transporting and hole blocking layer (ETL/HBL) as shown in Table 3. A commonly used [22,28,36,37,58] and solution processable material is zinc oxide (ZnO). Other options are titanium oxide (TiOx) and the polymer PFN.
These are discussed in the following sections.

2.4-I A) ZNO

Zinc oxide (ZnO) has properties that are very useful for an electron transport layer in our configuration. It is a wide bandgap semiconductor with a low-lying valence band so that excitons and holes cannot be transported and will be blocked. Also, the conduction band level (-4.2 eV [59]) is situated between the LUMO level of PCBM (-3.7 eV [28]) and silver (-4.3 eV [59]) which indicates that it could form an Ohmic contact as is desired.

The resulting device architecture is shown in Table 3. An energy level diagram of the resulting structure (with the ITO replaced by the 'Holst' anode consisting of a silver grid with high-conducting PEDOT:PSS on top) is shown in Figure 16. This diagram clearly shows that ZnO is a very suitable material for this purpose. ZnO has been shown to perform very well in different device architectures [28,35–37,60,61].

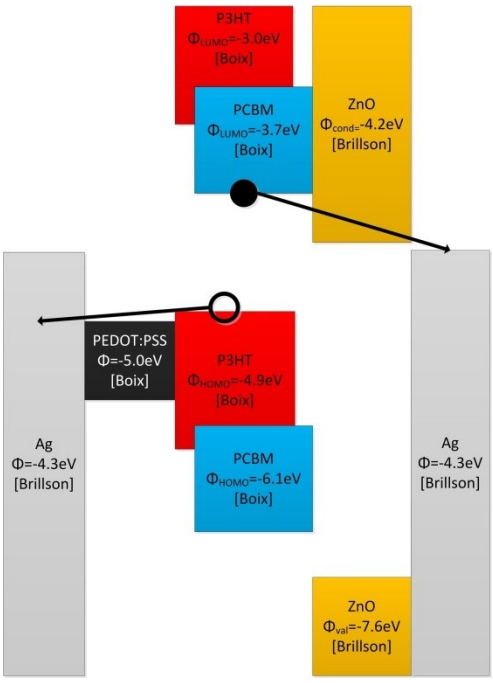

Figure 16 – Energy Level Diagram of the final goal: an "all solution processed" design. Sources: Brillson: [59] **Boix:** [28]

For this report the ZnO layer has been processed using two separate methods. The first method is based on the precursor zinc acetylacetonate ($Zn(acac)_2$). This material can be dissolved in alcohols and can thus be processed on top of the organic layers. It should react at low temperatures with atmospheric water [60] to form ZnO, but it is known that high humidity's are required for a fairly complete conversion (above 3.2 kPa partial pressure, which is above saturation at room temperature [62]). The second method is based on ZnO nanoparticles (this design will be abbreviated as *npZnO*) which can be spincoated as-is from acetone or isopropanol. Further details are given in the experimental section.

Often an S-shape (see section 2.2-I B) appears in the *J-V* curves when using ZnO [33,37,60]. This can often be solved by using UV-illumination. UV-illumination can excite electrons from the ZnO valence band to the conduction band which in turn can cause the desorption of oxygen from the ZnO [63] which increases the amount of mobile electrons in the conduction band for a longer period. This can increase the energy level of the conduction band and thus change the alignment of energy levels between the layers.

2.4-I B) Titanium Oxide

Titanium Oxide (TiOx) is a material which is very similar in electronic structure to ZnO. It is a wide-bandgap semiconductor with a valence band at -8.0 eV and a conduction band at -4.3 eV [40]. It has been shown to work in as an ETL as desired [40,64]. It can be processed in a sol-gel or using nanoparticles. The sol-gel route is currently work-in-progress at Holst Centre and could not be used yet. A solution based on nanoparticles derived from a sol-gel (unpublished thus no further details are available) was obtained from IMEC – however, the process could not be successfully transferred to our labs.

2.4-I C) PFN

The polymer PFN (poly[(9,9-bis(3′-(N,N-dimethylamino)propyl)-2,7-fluorene)-*alt*-2,7-(9,9–dioctylfluorene)] [65], Figure 17) has been used in OLEDs [66] and OSCs [67] as a cathode interlayer. It is known that it reduces the barrier height for electron transport and increases the barrier height for hole transport and thus functions both as an ETL and a HBL. The effect of PFN is explained by the formation of a dipole layer because the polar amino groups have a strong interaction with the metal electrode and thus align [68,69]. This dipole causes a vacuum energy level shift and can thus increase alignment of the energy levels between PCBM and the silver cathode, as previously explained in section 2.3-I and Figure 14. The fact that its function is based on an interfacial property (dipole at surface) and not a bulk property (e.g. wide bandgap semiconductors) means that the layer should be as thin as possible, because extra thickness does not add to the effect and only causes a higher series resistance.

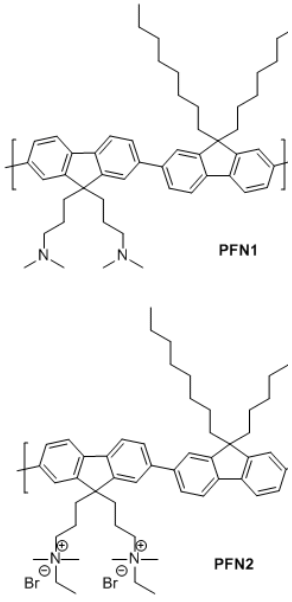

Figure 17 - PFN1 and PFN2

PFN can be synthesized in two forms: the neutral PFN1 and the quaternized PFN2 [65] (Figure 17). The solubility is different for both materials. PFN1 can be dissolved in organic solvents like chloroform and alcohols when a small amount of a weak organic acid is added. PFN2 cannot be dissolved in chloroform but can be dissolved in alcohols. The fact that alcohols can be used is beneficial, because it can then be processed on top of the organic layers. The total cell designs will be abbreviated as *PFN1* and *PFN2*.

2.4-II SELF-ASSEMBLED MONOLAYERS

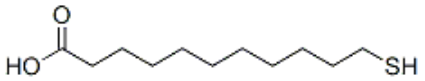

Figure 18 – 11-mercaptoundecanoic acid (MUA)

It has been reported that it is possible to insert a monolayer on top of ZnO using a carboxylic acid which binds to the ZnO [70]. The dipole caused by the monolayer shifts the vacuum energy levels and thereby could align the energy level of the ZnO conduction band with the silver electrode and improve charge transfer properties of this interface. The dipole consists of two parts: (1) the bond dipole, which is caused by the silver-monolayer bond formation and (2) internal dipole moment of the monolayer molecules [71]. In our case the energy level of silver cathode should be shifted up relative to the PCBM (see Figure 16), which means the dipole of the monolayer molecule should point from the silver towards the ZnO. Also, it would be beneficial if the bond dipole caused by the bond formation between the molecule and the silver would point away from the silver. This is the case for –SH terminated molecules [71]. Thus a good option would be 11-mercaptoundecanoic acid (MUA, see Figure 18), of which the beneficial effect indeed has been shown [70]. For this project the most important effect is that the surface properties will also change, which influences the deposition of the silver ink on top of the ZnO | MUA layer.

2.4-III SILVER PRINTING

The main option for the deposition of a silver electrode which is regarded in this project is inkjet printing. Silver inks usable for inkjet printing should follow three requirements [72]:

1. Very low viscosity
2. Behave as a *true solvent*, which means that the solvent must not separate from the silver in accelerating drops
3. Be able to convert into conductive structures

There are mainly two solutions that fulfill these properties: nanoparticle suspensions or silver-complex solutions which will be explained in the following sections. Other deposition methods for silver inks include slot-die coating of silver complex solutions and screen printing, but these have not been used in this project.

2.4-III A) NANOPARTICLE SUSPENSIONS

For inks based on small silver particles the *true solvent* condition implies that the particles should be small – that is tens of nanometers. That means that the nanoparticles should also be prevented from agglomeration when suspended in the final ink. This is done by creating a polymer shell around the silver nanoparticles. However, if the ink is then printed and the solvent has evaporated, the nanoparticles will be surrounded by an insulating polymer shell. This shell is removed by a heat-treatment which is called *sintering*. Continuing heat treatment enlarges the contact area between the nanoparticles by *Oswald Ripening* [73] which increases the conductivity further.

A lot of work has been done and development is still ongoing to reduce the sintering temperature and time. Previously silver inks required sintering temperatures well above 150°C, which is above the glass transition temperature of commonly used substrate foils. The current generation of silver inks can already be sintered at 120°C during 20 minutes, which is compatible with polymer foils. Ongoing work at Holts Centre involves for example the required sintering time, which is to be reduced to allow for roll-to-roll processing. This is for example done using microwave sintering and photonic flash sintering [19,73].

2.4-III B) Silver Complexes

Silver complexes (for example silver neodecanoate [74]) can be dissolved in organic solvents. The fact that the complexes dissolve (compared to a suspension) has the advantage that it will always behave as a true solvent and that the ink is very stable. However, to form conductive structures an entirely different mechanism has to exist. Most often a heat treatment is used, but the exact mechanism is not always known and depends on the used complex. The end-product of the chemical reaction has to be elemental silver. The silver atoms will then bind together to form a conductive silver layer.

3 EXPERIMENTAL

The first section contains the instrumental details used for the characterization of the solar cells. After that a series of sections is devoted to the layers used in the cells in the order of preparation.

3.1 CHARACTERIZATION

The measurement of *J-V* curves has been done in both simulated sunlight conditions and in the dark. A voltage sweep from -2 to +2 Volt was done using a Keithley 2400 source meter. The sunlight was simulated using a tungsten halogen-lamp setup with a Schott GG385 UV-filter and a Hoya LB120 daylight filter. It has been calibrated to ~100 mW/cm^2 using a silicon reference cell. Measurements were performed using a mask to obtain a well-defined illuminated area. The mask areas were 0.04, 0.09, 0.25 and 0.81 cm^2 for respectively the A, B, C and D cells.

The External Quantum Efficiency (EQE) shows how many incident photons are converted into electrons and extracted from the devices at 0 V bias. The EQE has been determined at Eindhoven University of Technology (TU/e) using a 50 W Philips focusline tungsten halogen lamp in combination with an Oriel Cornerstone 130 monochromator. The lock-in amplifier (Stanford research Systems SR830) measured the response as a voltage over a 50 Ω resistance. These measurements were converted to EQE by comparing the measurement with a silicon reference cell. A green laser bias light was available to use realistic charge generation conditions.

Atomic Force Microscopy (AFM) measurements were performed by René Beerends (Philips Innovation Services) using a Bruker Nano Dimension 3100 scanning probe microscope with a Si probe in tapping mode. The scan range was set to 5×5 μm^2 and 512x512 data points were recorded. Surface roughness values R_a and R_q are obtained from height data after background correction. Conductive AFM (C-AFM) was done using the same setup, but now with a Pt/Ir coated tip in the contact mode and a DC sample bias of +500 mV.

Scanning Electron Microscopy (SEM, Zeiss Supra 55VP) measurements were performed by Jack Hoppenbrouwer (Philips Innovation Services). The SEM could also perform local Energy-dispersive X-ray spectroscopy (EDS, Oxford instruments X-Max 80 with INCA and Aztec software) to obtain a spectrum which contains information on the elemental composition of the sample.

A cross-sectional Transmission Electron Microscopy (TEM) measurement was done by Marcel Verheijen (Philips Innovation Services). The sample was prepared by Hans Bolten using a Nova 200 Nanolab SDB (SDB stands for Small Dual Beam). Before preparation, a thin Pt layer is deposited using electron beam induced deposition (EBID) and a 1.5 μm Pt layer is deposited using ion beam induced deposition (IBID) on the region of interest to protect the sample during preparation. TEM studies were performed using a TECNAI F30ST TEM operated at 300kV.

Thicknesses as indicated were always measured using a Veeco Dektak profilometer on a glass substrate.

Thermography measurements were made with a lock-in infrared camera, a Thermosensorik CMT 384SM. Lock-in settings are 132 frames/period with a frequency of 1.0 Hz. When a negative bias is applied the current should only flow through the shunts. These shunts then heat up due to the current. This can be shown in either an assembled image of multiple measurements or a phase image which shows how long it takes for shunts to heat up.

3.2 BOTTOM ELECTRODE

The substrate was always a 30x30mm glass plate. The bottom electrode was always patterned for four different cell areas (which will be defined by the overlap of the bottom and top electrode) and was thus called an "ABCD" design. The cell areas are 0.090, 0.160, 0.360 and 1.00 cm^2 respectively. The bottom electrode was a sputtered and patterned Indium-Tin-Oxide (ITO) layer or a printed silver grid.

The ITO substrates were bought from Naranjo and cleaned with the following procedure: 10 minutes sonication in acetone, then scrubbing with soap in deionized water and also 10 minutes sonication in this solution. Then the soap is removed through a cascade bath. The final step is 10 minutes sonication in isopropanol and the surface is then prepared for spincoating using a 30 minute UV-ozone treatment. On top of ITO the hole transporting layer poly(3,4-ethylenedioxythiophene):poly(styrenesulfonate) (PEDOT:PSS, Clevios 4083) - which was filtered using a 0.45 µm PVDF filter - was spincoated (60 seconds, 3000 rpm, acceleration: 1000 rpm/s, closed). This layer was dried at 130°C for at least 10 minutes. The process results in a layer thickness of 10-15 nm.

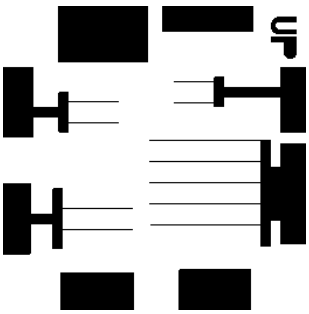

Figure 19 - bottom grid

The grids were printed by myself on a Dimatix DMP-2800 using Suntronics U5714 silver ink from 10 pL cartridges. Glass plates with a SiN layer were thoroughly cleaned using the same procedure as for ITO. Before silver printing a 1000 Watt oxygen plasma was applied for two minutes in a Tepla 400. The cartridge temperature was set to 30°C and the substrate was at room temperature. A drop spacing of 40 µm was used. The grids were sintered at 190°C for at least 30 minutes. The resultant grid lines have a height of ~300 nm and a width of ~150 nm. The pattern was chosen so that all grid lines were in the x-direction for the printhead movement (see Figure 19). On top of the grid a high-conducting PEDOT:PSS formulation (Agfa HILHC5 IJ) was inkjet printed by Harrie Gorter using a Spectra Galaxy printer. Before printing a 1000 W nitrogen plasma was applied in a Tepla 400 for 3 minutes. The drop volume was ± 24 pL and the drop pitch was 10x100 µm. The solid content of the ink was 1.1% and thus the resulting average layer thickness was ~260 nm. However, as can be seen in the Dektak scan shown in Figure 20, the thickness is not uniform but varies from 100 – 300 nm.

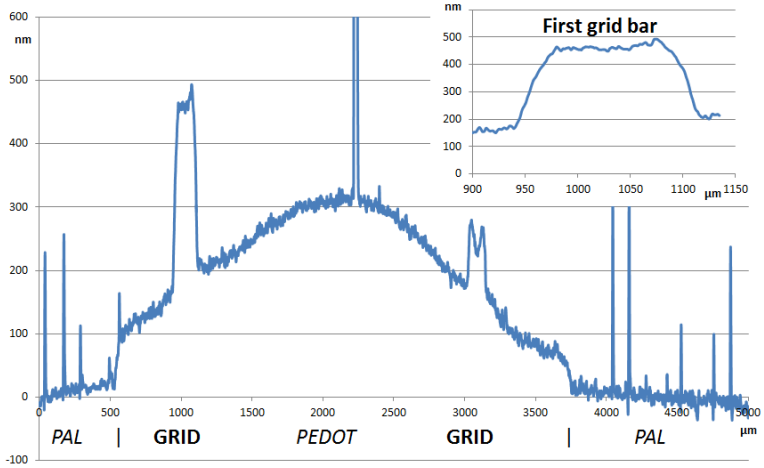

Figure 20 - Dektak scan on top of the whole stack

3.3 PHOTO-ACTIVE LAYER

The photoactive layer (PAL) was always the same, because we were interested in the effect of the interfacial layers. The solution consisted of 26 mg of poly(3-hexylthiophene) (P3HT, Plextronics OS 2100) and 26 mg of [6,6]-phenyl C_{61}-butyric acid methyl ester (60-PCBM, Solenne) in ortho-dichlorobenzene (oDCB). This was stirred vigorously at 65°C during one night. Before spincoating the solution was filtered through a 5.0 µm PTFE filter using a plastic syringe, which could cause some silicone contamination [75] – this did not noticeably affect the photovoltaic performance but may affect the surface properties. The layer was then spincoated using the heated solution (65°C) during 60 seconds at 1000 rpm (acceleration: 1000 rpm/s, closed). Further processing was done after drying in air until visibly dry (at least 5 minutes). Devices with evaporated cathodes were annealed for 10 minutes at 130°C in a nitrogen glovebox just before evaporation of the silver (so after application of the cathode interlayer). For solution-processed cathodes the heat treatment was more complex because the silver cathode also requires sintering. The resulting layer thickness is 200-250 nm.

3.4 CATHODE INTERLAYER

The cathode interlayer was one of the important parts to realize the solution-processable cathode. Therefore a lot of different options have been tried, which are detailed in separate sections.

3.4-I $Zn(acac)_2$

The ZnO precursor $Zn(acac)_2$ was used in two different solvents: ethanol and pentanol. From ethanol it was not possible to obtain reproducible results, probably because it should be spincoated on a heated substrate, which is a difficult manual procedure. When using pentanol we were able to obtain reproducible but no satisfying results. A concentration of 20 mg/mL was used. After stirring the solution was filtered using a 0.45 µm PVDF filter and spincoated at 1000 rpm (acceleration: 1000 rpm/s, closed) during 60 seconds. Then, after at least 30 minutes, it was put on a 130°C hot plate in air for 30 seconds to convert the precursor into ZnO.

3.4-II ZnO NANOPARTICLES

Zinc oxide nanoparticles (~5 nm diameter) were synthesized by Pim Voorthuijzen. He used a modified sol-gel process based on [76] and [77]. The nanoparticles were dispersed in a isopropanol or acetone in a concentration of 10 mg/mL. They were spincoated at 1000 rpm (acceleration: 5000 rpm/s, open) during 60 seconds. The isopropanol based-solution wetted very well, but was not stable and resulted in non-closed layers. The wetting for the acetone based-solution was also good, but due to very fast drying always coffee rings were visible. It was ensured that a large enough drop was used to cover all active area, so that the coffee ring would not affect results. The resulting layer thickness is in the range of 20-40 nm, but is very difficult to determine.

3.4-III TiOx

Titanium oxide nanoparticles were prepared in solution by Afshin Hadipour (IMEC) using a non-published and confidential sol-gel process. They were supplied for testing. The isopropanol-based dispersion should be diluted to a concentration of 0.5–2 wt%. We were not able to obtain an improved performance using this solution, because we observed dewetting “craters” after spincoating (1000 rpm, acceleration 5000 rpm/s, 60 seconds, open). Craters are often caused by spots with a lower surface energy [78] and thus might be related to the silicone contamination in the photoactive layer [75]. This problem could not be solved in the timeframe of this project.

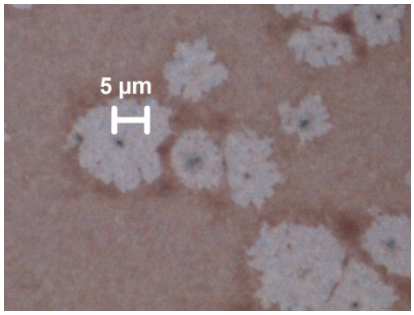

Figure 21 - TiOx dewetting "craters"

3.4-IV PFN

PFN (poly[(9,9-bis(3´-(N,N-dimethylamino)propyl)-2,7-fluorene)-*alt*-2,7-(9,9–dioctylfluorene)) was used in two forms: PFN1 and PFN2 (see section 2.4-I C). PFN2 was supplied by 1-material and dissolved in a concentration of 0.4 mg/mL in ethanol. PFN1 was synthesized by Koen Hendriks using the method in [65] and was used in a concentration of 0.5 mg/mL in ethanol, with 0.01 mL of added acetic acid to help it dissolve. Both were spincoated at 1000 rpm (acceleration 5000 rpm/s, 60 seconds, open). The resulting layer thicknesses cannot be determined using a Dektak.

3.5 ADDITIONAL "INTERLAYER"

Two types of interlayers have been used on top of the nanoparticle ZnO layer. One is derived from tandem cells made by Jan Gilot [36,37] and is based on a neutral PEDOT:PSS formulation supplied by Agfa. This was spincoated at 1000 rpm (acceleration 1000 rpm/s, 60 seconds, closed). However, this always caused shorted cells after annealing all through the active area (see Figure 22) and was thus not suitable to use in combination with a printed silver ink that requires sintering.

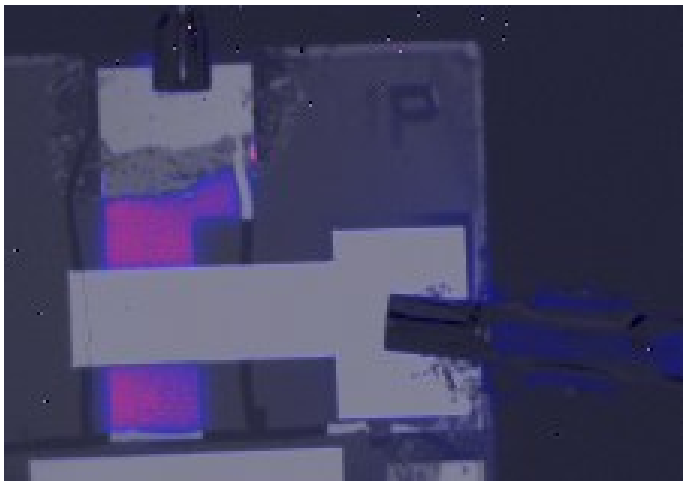

Figure 22 - Thermography reveals shunting caused by high-conducting PEDOT

The other interlayer was a Self-Assembled Monolayer (SAM) of 11-mercaptoundecanoic acid (see section 2.4-II). This molecule was dissolved in a concentration of 0.011 gram in 5 mL of ethanol. It was then spincoated at 1000 rpm (acceleration 1000 rpm/s, closed, 20 seconds). Then a drop of pure ethanol was spincoated using the same settings to remove non-assembled molecules.

3.6 CATHODE

Three different cathodes were used: the “reference” LiF|Al, evaporated silver and printed silver. Each is described in a separate section.

3.6-I LiF|Al

The reference electrode was evaporated using Physical Vapor Deposition (PVD). The manual process was started after the pressure reached a value below $2*10^{-6}$ mbar. First 1 nm of Lithium Fluoride (LiF) was evaporated at slow rates (0.025 nm/s) using ~50 A of current. Then the aluminum was evaporated with a current between 60-70 A at a rate between 0.15 and 0.35 nm/s.

3.6-II Evaporated silver

Silver was also evaporated using PVD. Again the process was started when the pressure reached values below $2*10^{-6}$ mbar. Silver is evaporated at ~85 A at a rate between 0.2 and 0.6 nm/s.

3.6-III Silver Printing

The solution processed cathode used printed silver. The used printer was a Dimatix DMP-2800 with 10 pL cartridges. A lot of different inks have been tried and compared, but the best results were obtained using Suntronics U5714. This is a nanoparticle ink which contains 40 weightpercent of silver nanoparticles with a size of ~30 nm dispersed in mainly ethylene-glycol. This is a polar solvent and can thus not be directly printed on the photoactive layer. However, on the cathode interlayer it can be printed. Sintering to remove the isolating polymer shell requires a temperature of 120°C. It will be conductive after ~3 minutes of sintering, but longer sintering times are required to further reduce the resistance.

Printing settings have been varied a lot and will be mentioned when relevant, but as a general starting point a drop spacing of 20 µm was used, along with a cartridge temperature of 30°C and a substrate temperature of also 30°C. Sintering was generally done during 20 minutes in an oven.

4 RESULTS

4.1 EFFECT OF ETL AND HBL

As explained in section 2.3-II and 2.3-III, the cathode modification layer should ideally transport electrons and block holes: it should both be an Electron Transport Layer (ETL) and a Hole Blocking Layer (HBL). This effect can be seen on the measurements in the dark and in the light on devices with an evaporated silver electrode.

An increased transport of electrons would show up by a lowering of the series resistance and an increase in current in forward direction. This effect is demonstrated by the dark current measurements of the two representative devices in shown Figure 23. In forward direction, at 2 V bias, the current is clearly higher for the device which incorporates the *npZnO* ETL/HBL. This is also shown in the series resistance as obtained from the fit to the diode equation: it decreased from 4.16 Ω to 3.04 Ω.

Better hole blocking capabilities should give a decreased dark current in reverse direction and a larger shunt resistance. The decreased dark current in reverse direction can clearly be seen in Figure 23 at -2 V. The shunt resistance increased from 964 Ω to 1457 Ω.

The increase of onset voltage (as an indication I used the value for which J_{dark} increase above 1 mA/cm^2) is related to the effects on open-circuit voltage. The onset voltage changed from 0.29 V to 0.44 V as was expected from the discussion in section 2.3-I. When a ZnO layer is inserted between the PCBM and the silver the alignment of energy levels will change and thus the onset voltage and open-circuit voltage retain their "normal" value.

All three effects are beneficial for the photovoltaic performance as shown in Figure 24. In this case J_{sc} increased from 10.0 to 10.5 mA/cm^2, the FF increased from 53.5 to 58.9% and the V_{oc} increased from 0.38 to 0.52 V. Finally, the MPP increased from 2.0 mW/cm^2 to 3.2 mW/cm^2.

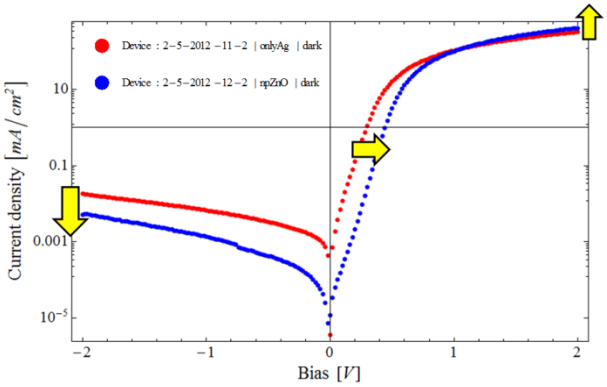

Figure 23 - Effects of ETL and HBL (red = *onlyAg*, blue = *npZnO*)

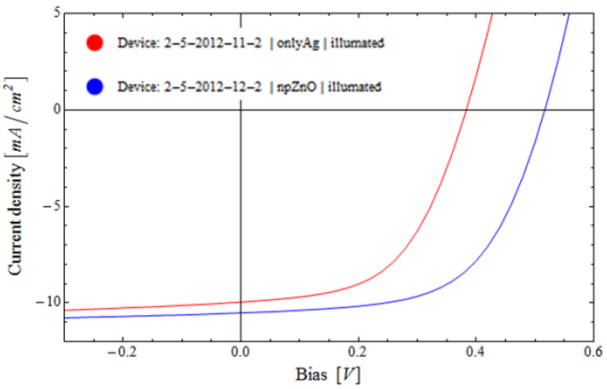

Figure 24 - Effects of ETL and HBL on photovoltaic performance

4.2 COMPARISON OF DEVICE ARCHITECTURES

To show that the effect in the previous section is not an isolated effect the average values have been calculated for all devices with evaporated electrodes which show reasonable performance (Table 4). Malfunctioning and severely underperforming devices are excluded from the average to give a view of the reproducibly archievable performances. Table 1, 2 and 3 in section 2.4 show the used designs. The drop in performance when going from the *Reference* design (LiF | Al cathode, Table 1) to the *onlyAg* (only a silver cathode, Table 2) is very clear. When either ZnO nanoparticles (*npZnO*) or PFN-1 (*PFN1*) are used as ETL (Table 3) the performance increases again to reasonable levels. The trends indicated in the previous section are thus also confirmed in general. The other investigated ETLs - ZnO prepared from $Zn(acac)_2$ (*Znacac*), TiOx from IMEC (*TiOx*) and *PFN2* - were all performing less, and are shown in the table too. *Znacac* results were not reproducible – this can be seen in the uncertainty in the V_{oc}. *TiOx* had wetting issues and therefore performed comparable with *onlyAg*. *PFN2* was better, but probably the concentration of the used solution was slightly too low to archieve the high performance of *PFN1*.

Table 4 – Average performance of different cell designs (see section 2.4 for structures). A reasonable selection has been made that excludes malfunctioning devices. The column 'based on' shows how many devices (with each 2 cells) are used in the average and the number of different series/production dates these devices belonged to. R_{series} and R_{shunt} have been calculated from the inverse slope of the *J-V* curve around respectively 1.75 V and 0 V.

	Based on	J_{sc} [mA/cm^2]	V_{oc} [V]	FF [%]	MPP [mW/cm^2]	R_{series} [Ω]	R_{shunt} [Ω]
Reference	6 | 2	9.0 ± 0.7	0.53 ± 0.01	67 ± 2	3.16 ± 0.22	2.6 ± 0.8	1380 ± 126
onlyAg	6 | 5	9.1 ± 0.5	0.38 ± 0.02	51 ± 3	1.79 ± 0.12	5.7 ± 1.8	421 ± 60
npZnO	20 | 12	9.8 ± 0.6	0.49 ± 0.03	57 ± 4	2.73 ± 0.32	2.8 ±1.4	878 ± 355
PFN1	2 | 2	10.3 ± 0.5	0.52 ± 0.01	59 ± 4	3.14 ± 0.34	2.7 ± 0.6	875 ± 210
PFN2	2 | 2	9.3 ± 0.5	0.49 ± 0.01	59 ± 3	2.70 ± 0.26	2.3 ± 0.9	705 ± 211
TiOx	11 | 5	9.0 ± 0.5	0.38 ± 0.02	52 ± 3	1.77 ± 0.15	5.3 ± 2.2	467 ± 105
Znacac	11 | 6	8.9 ± 0.7	0.44 ± 0.05	49 ± 5	1.92 ± 0.40	3.9 ± 2.1	423 ± 161

Performance can vary on day-to-day (=batch-to-batch) basis. Possible causes are slightly different solution concentration, the age of the solutions, the humidity, the calibration of the measurement setup, the pressure or rate during evaporation and the experimenters experience with the equipment. This effect can especially be seen in the uncertainty for *npZnO*, for which a lot of cells have been made. Good batches perform almost the same as *Reference*, but bad batches can perform far worse. To elucidate some of these effects a direct comparison of devices made in the same batch is shown in Figure 25: it is clearly visible that the fill factor and V_{oc} are consistently different and the current is consistently the same. This shows that the averages and the corresponding differences in the J_{sc} and accordingly the MPP cannot be used reliably because that is expected to depend more on calibration issues and active layer thickness than on the device structure. However, the uncertainty in both the FF and the V_{oc} are quite small and thus can be used to compare different structures.

For *npZnO* the variation in V_{oc} is relatively large – this can be explained by difference in age or pre-spincoat sonication of the nanoparticle dispersion. This was largely solved by the switch from an isopropanol based dispersion to an acetone based dispersion – that was much more stable. If the averages are calculated only for devices prepared from acetone the V_{oc} is 0.51±0.02 V and the FF is 59±2 %. This is comparable with the results for *PFN1.* In Figure 26 also a direct comparison is shown between *npZnO* and *PFN1*. This shows the two ETLs have the same potential.

When this discussion is combined with the data in Table 4 a conclusion can be drawn regarding the different device architectures. When the apparent difference in J_{sc} is not included, the *Reference* device always performs best. However, both *PFN1* and *npZnO* achieve the same V_{oc} and only a 12% lower FF (67% vs. 59%) and thus the loss in photovoltaic performance will also be 12% (assuming the same current) – this loss is acceptable when compared to a device with only a silver cathode, which performs 43% lower than the *reference* device. It should be noted that an ETL can also act as an "optical spacer" [64], which could optimize the absorption of light inside the photoactive layer and therefore increase the current. This effect has not been taken into account because the uncertainty in current is expected to be of the same magnitude as this effect. If the effect would be relevant, it would show up in the J_{sc} shown in Figure 25.

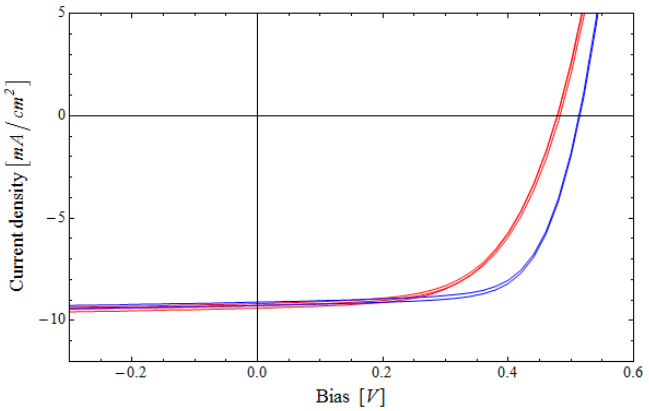

Figure 25 - Direct comparison of the A-cells on two *reference* devices (blue) with three *npZnO* devices (red) all made on 15-03-2012

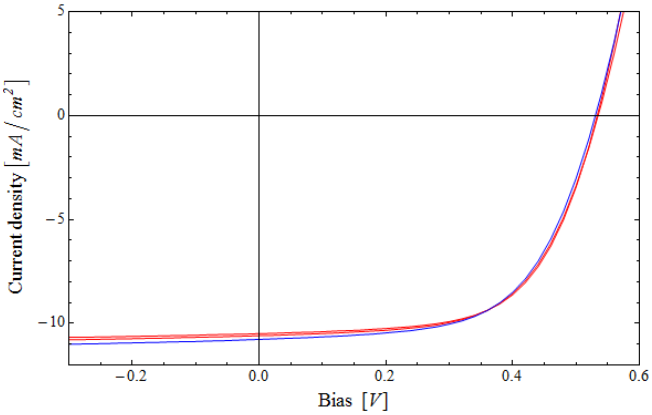

Figure 26 - Direct comparison of the B-cell on one *PFN1* (blue) device with two *npZnO* devices (red) both made on 30-05-2012

4.3 PRINTED CATHODE

The previous sections show that it is possible to use silver as a cathode instead of the "usual" aluminum. This indicated that it should be possible to produce a solution-processed cathode, because commercial silver inks are available. In the section above there are two good options – *npZnO* and *PFN1* as interlayers. However, chronologically, *npZnO* was the first option and thus research focused on printing of silver on top of ZnO nanoparticles which will be discussed in the following section. Only later it was discovered that PFN might be more suitable and that is discussed in a separate section.

4.3-I PRINTING OF SILVER ON ZNO NANOPARTICLES

The first try of printing with the "default" ink (Suntronics U5714) on top of the ZnO nanoparticles looked promising. Wetting was good and closed layers were formed. However, devices were not working because no current was transmitted at all. Microscope images quickly revealed the cause: cracks were formed during sintering of the silver ink. The application of a silver paste on top of the cracked silver layer gave even more promising indication: a working cell was made, however the performance was very low: ~0.41 mW/cm^2.

Figure 27 - Microscope image (50x) of cracks in silver

The research then focused on the prevention of crack formation. This ink does not crack when processed on glass using exactly the same settings, so it might be that just a small change could prevent cracks. Cracks can be caused by too fast drying [79] and thus the first option was reduce the drying rate. It was attempted to first dry at lower temperatures before sintering at 120°C and to leave the sample to dry overnight before sintering. None of the options worked and cracks already formed at 80°C.

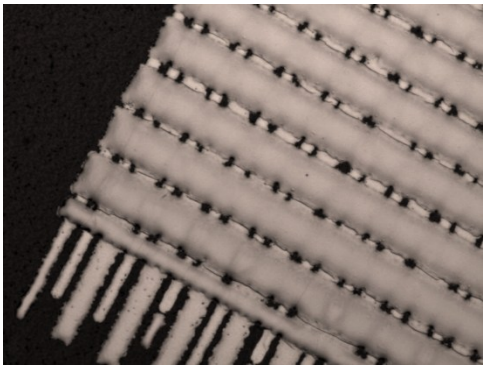

Figure 28 - Almost no cracks in grid pattern (50x)

It is known that thinner layers are more flexible than thicker layers. It is also known that thin lines have less tendency to crack than full areas or thicker lines [80]. Thus it was attempted to obtain thinner layers by increasing the drop spacing. This was done past the critical limit were the lines do not connect anymore and thus stripes are printed. All closed layers still cracked, but in the lines almost no cracks appeared because they have more freedom of movement and can thus more easily relief stresses without cracking. It was thus tried to print a grid pattern by printing twice (see Figure 28). This again showed it was possible to obtain working cells with printed silver. Performance was still not good but two cells reached over 0.51 mW/cm^2. This again showed that it should be possible to succeed if only cracks could be prevented.

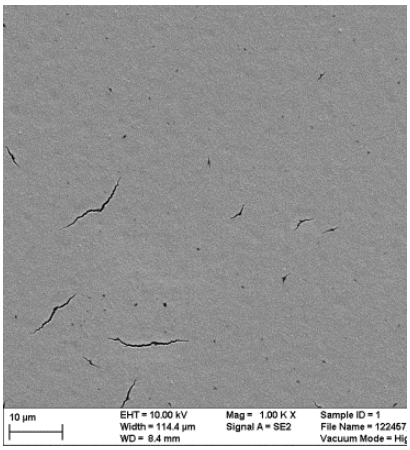

Figure 29 - SEM image of thin and non-conducting silver

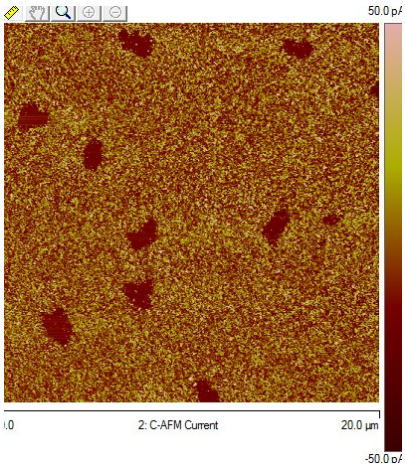

Figure 30 - Conductive AFM on non-conducting silver, 20x20 µm

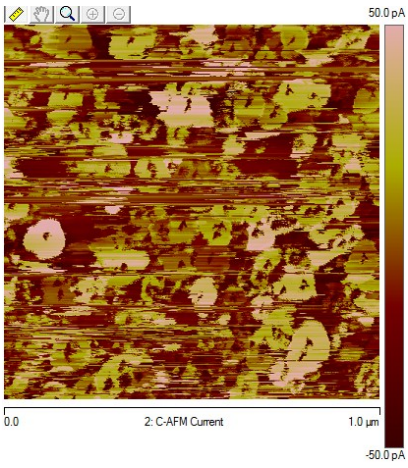

Figure 31 - Conductive AFM on non-conducting silver, 1x1 µm

Even thinner layers were made using Suntronics U5604 ink – that is essentially the same ink, only the silver concentration is decreased to 20% so layers will be half as thick. When this was combined with the highest possible drop spacing for closed layers (35 µm) it was possible to obtain a layer that did not crack all through – only small cracks were formed (see Figure 29). The thickness was around 250 nm, but it did not conduct. Layers this thick on glass did conduct very well, so this was not understood. Conductive AFM was performed in an attempt to explain this (Figure 31). In conductive AFM a current is measured between the AFM probe and a layer of applied silver paste. The current pathways are indicated by the yellow arrows in Figure 32. A short distance (~1 µm) away from the silver paste the current (~50 pA) was already much lower than the current that was measured directly on the silver paste (> 50 nA). Going further away (up to 1 mm) did not decrease the current, thus the resistance was very high but did not depend on distance. This indicates that the current is contact-limited and a possible explanation is given in Figure 32: the measured current is actually not going through the silver layer, but through the ZnO layer. This is also supported by 20x20 µm scans with the conductive AFM (Figure 30), in which micrometer-sized non-conducting spots appear. We know from SEM images that there can exist these kinds of holes in the ZnO layer (Figure 36). The fact that the silver layer did not conduct is then caused by the visible variation between 'conducting' and 'non-conducting': separate silver domains are formed but not connected. Why this happens is not known yet, but there are indications from later experiments (the stacks *glass | ZnO | silver* and *PAL | ZnO from cyclopentanol | silver*) that conduct, but with higher resistances and/or longer sintering times than either silver on glass or on PFN. This indicates there might be some interaction between the ZnO and the printed silver but time did not allow to investigate further.

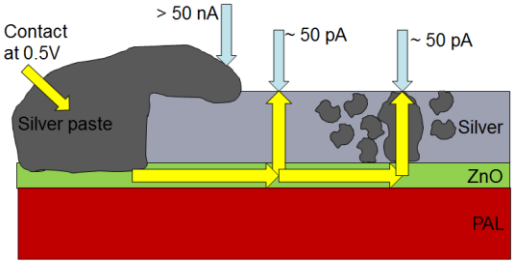

Figure 32 - Measured current in C-AFM through low-conducting ZnO but limiting step is the 'upward' current through silver – that can only happen when the silver forms a connecting pathway, where it often does not.

The next option was the modification of the ZnO surface. It was attempted to apply a MUA monolayer (section 2.4-II). It was observed that less cracks are formed and the resistance decreased from "infinity" to values in the kΩ range. This is still far too much to obtain working devices.

Then also different silver inks were tried in a quick comparison. The two most promising were Harima NPS-JL (which is also based on a nanoparticle dispersion, but now in an a-polar solvent) and InkTec Tec-Co 011 which is a precursor-based ink in isopropanol, suitable for slot-die coating instead of inkjet printing. Further testing revealed that the Harima ink also did not work because of cracking, even when directly applied on the photoactive layer (which is not possible for Suntronics ink, because of the polar solvents). The InkTec ink could only be applied by spincoating and showed a good conduction. However, all devices were shorted at multiple points (see Figure 33). This did not mean the ink was unusable, but too complicated to process with spincoating on top of a device.

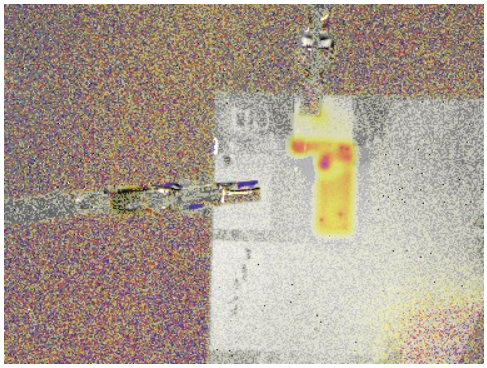

Figure 33 - Thermography phase image reveals multiple shorts for InkTec ink

All these experiments indicated that the crack formation was not a small problem, but a lot bigger than previously thought. The exact cause of cracking was still not known, thus the focus shifted towards the explanation of the crack formation. First, it was tried to print the Suntronics ink only on ZnO – that is without the photoactive layer underneath. Then no cracks were formed and the layer conducted. This is not strange because in the whole stack there will be thermal stresses in both the PAL (packing, crystallization) and the silver (drying, Oswald ripening) and the obvious layer to crack is silver, because that has a free surface – these double stresses will be absent when the PAL is left out.

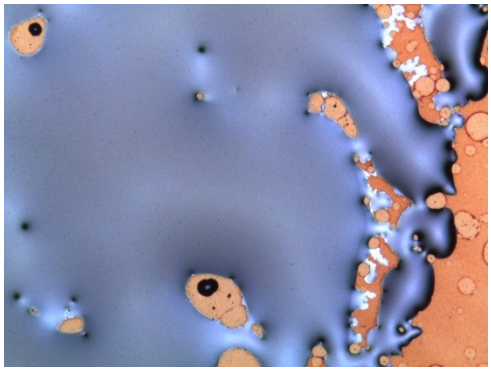

Figure 34 - Silver printed on bad-wetted TiOx layer

However, it was also tried to print silver on a glass plate with the photoactive layer covered with the bad-wetting TiOx obtained from IMEC. The silver ink dewetted from the non-covered areas as expected. However, on the areas where the coverage was good a nice layer formed that did not crack and conducted very well (see Figure 34). These two experiments indicate that the problem is not related to the ZnO or the PAL only, but to the combination of the photoactive layer with the ZnO (Table 5).

Table 5 –The problem is the combination of ZnO with the photoactive layer

Silver	Silver	Silver
TiOx	ZnO	ZnO
PAL		PAL
Glass	Glass	Glass
✓	✓	✗

To obtain some visible information on the processes happening at the interfaces we decided to acquire SEM images (Figure 35) and a cross-sectional TEM image (Figure 37) of a cracked silver layer. These showed the layer with ZnO nanoparticles was not closed. We thought this might be the problem and this was the reason to switch from an isopropanol based solution to an acetone based solution. New SEM images (Figure 36) on the ZnO layer which is on top of the PAL revealed that the ZnO layer was almost closed now – however, this did not resolve the cracking.

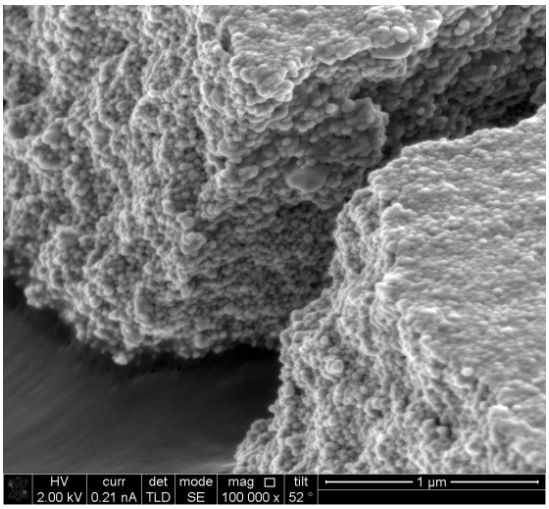

Figure 35 - SEM image of a crack – the stress in the underlying polymer layer indicates good adhesion between the layers.

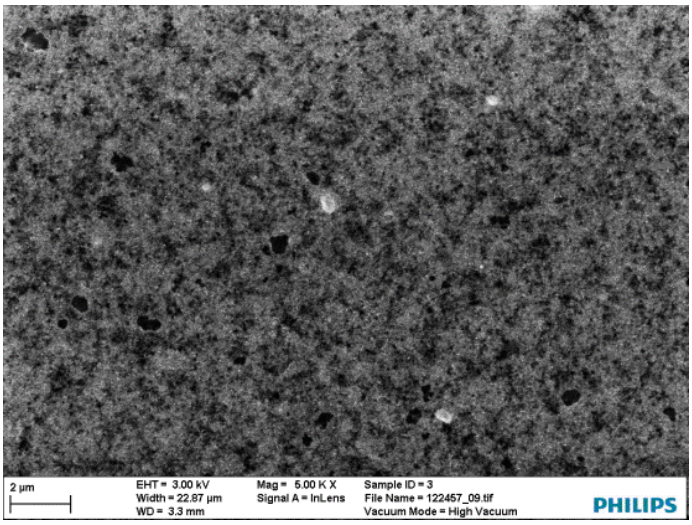

Figure 36 - SEM image of ZnO processed from acetone

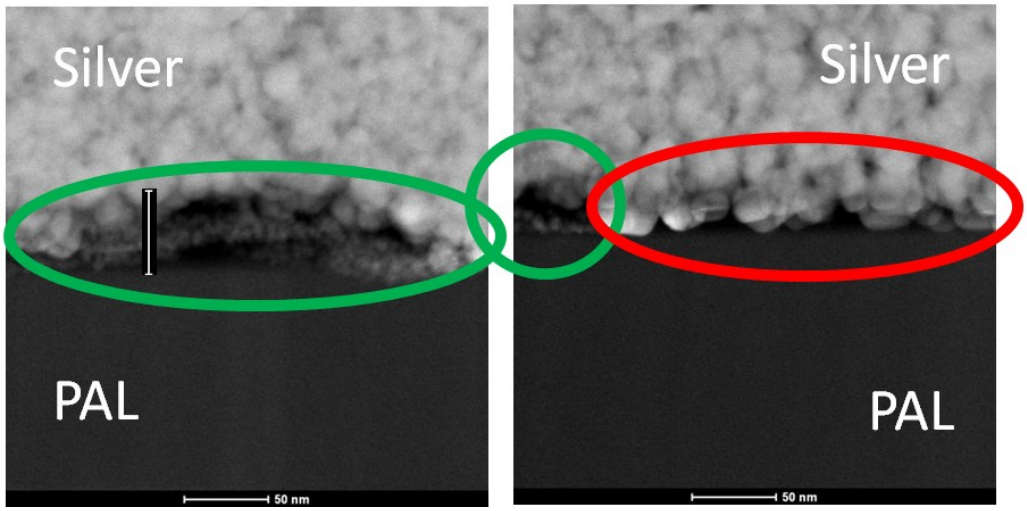

Figure 37 - Cross-sectional TEM shows the ZnO nanoparticle layer (green circles) is not closed (no ZnO within red circle). This has been confirmed by EDS.

AFM roughness measurements have been done on the same stack (photoactive layer with on top of that ZnO processed from acetone). This is shown in Figure 39 – it immediately shows that there are "spikes" of ZnO present. These "spikes" are probably ZnO nanoparticles that have aggregated either in the solution or during spincoating. The aggregates can have a diameter of ~200 nm and a height of ~100 nm. It is known and shown in Figure 38 and Figure 41 that the polymer photoactive layer which is beneath the ZnO deforms on heat treatment – the height differences are smaller afterwards. Figure 42 shows that also the height of the ZnO aggregates is decreased after 20 minutes on a 130°C hotplate in air (simulated "sintering"). This is also shown in the roughness parameter R_q (the root mean squared height) which decreases from 18.0 nm to 10.6 nm. It is noted that the ZnO layer has a lower roughness than the other two. This might be due to a smoothing effect of ZnO, but could also be caused by the fact that the ZnO sample has been processed on a different day op top of a PAL processed from a different solution.

These changes in roughness and thus form always happen in the photoactive layer. However, as is shown by the comparison with PFN in Figure 40, the "spikes" are unique to the ZnO layer. The combination of deformation with spikes could induce stresses in the silver which will be on top of this layer during heat treatment. This hypothesis is

schematically indicated in Figure 44. Before sintering, the red area is the photoactive layer, with on top of the ZnO nanoparticle layer with two drawn aggregates. On top of that is the printed silver. When this stack is sintered, the roughness of the photoactive layer will decrease (yellow arrows). Because of this, some ZnO aggregates will move partially sideways (green arrows) and down, which causes lateral stresses in the silver layer (red arrows) which cause a crack to appear (black arrow).

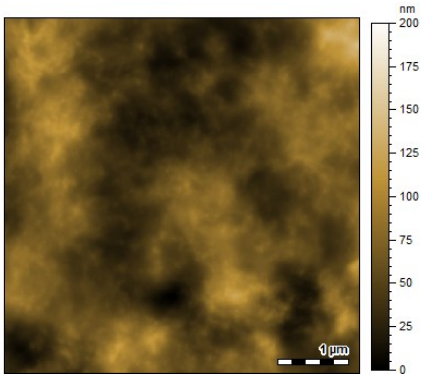

Figure 38 - AFM reference of PAL - R_q = 23.4 nm

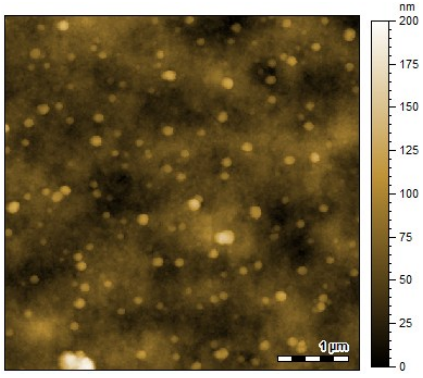

Figure 39 - AFM on ZnO layer - R_q = 18.0 nm

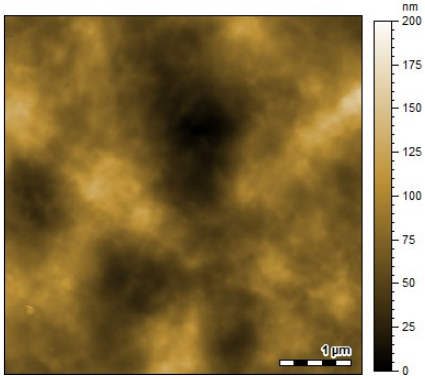

Figure 40 - AFM on PFN – R_q = 23.5 nm

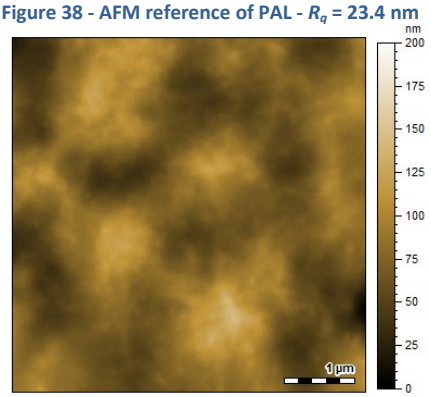

Figure 41 – AFM “sintered” PAL - R_q = 20.4 nm

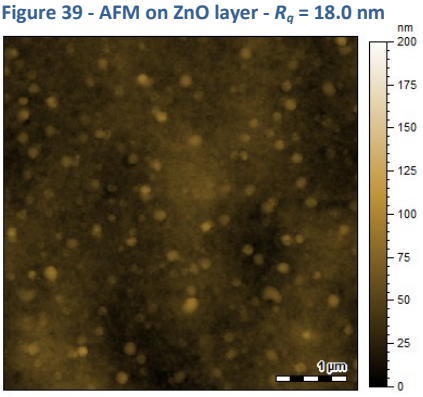

Figure 42 - AFM "sintered" ZnO - R_q = 10.6 nm

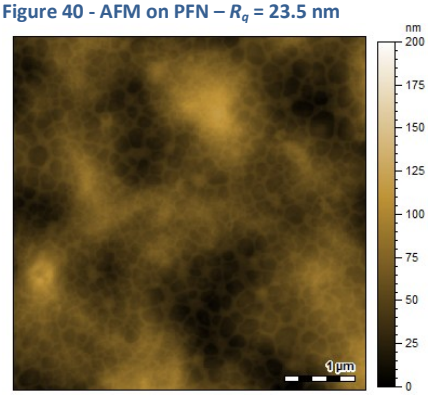

Figure 43 - AFM on “sintered” PFN - R_q = 19.2 nm

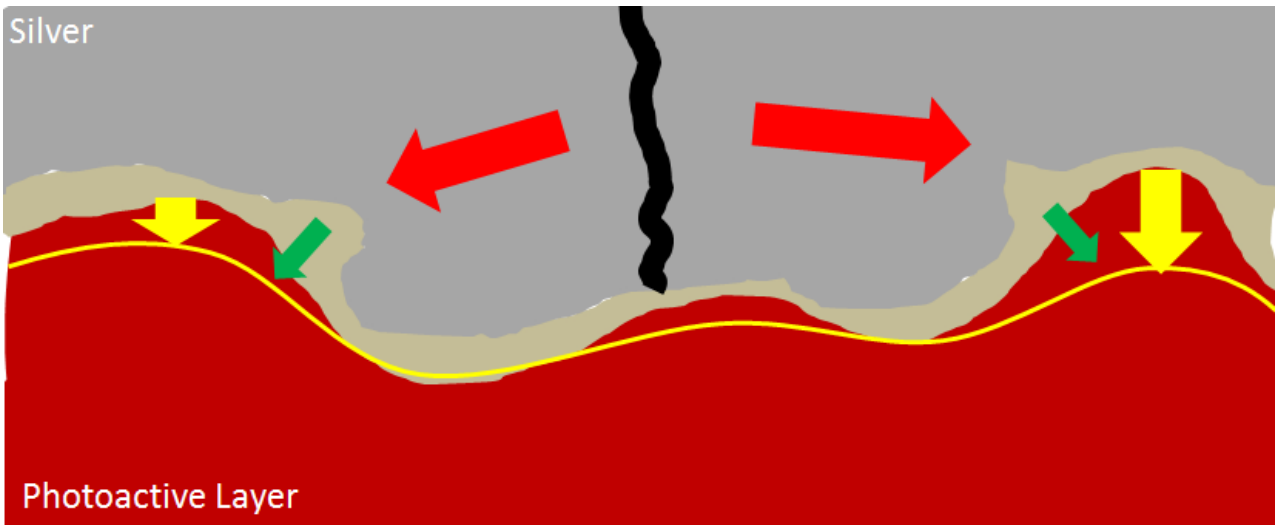

Figure 44 - Schematical indication of stresses formed in silver layer due to combination of PAL deformation with ZnO aggregates

A different hypothesis for the crack formation is that the cracks do not begin in the silver, but originate in the ZnO layer itself. It is known that ZnO is brittle [81] and can form cracks in thick dye-sensitized solar cells [82]. If the ZnO layer itself would form cracks than the silver layer on top of that could also crack with it.

Regarding the AFM on PFN, in Figure 43 an interesting effect appears. After “sintering” domains appear in the PFN layer. This might be related to the effects shown in Figure 54 and Figure 55 and cause the current to decrease. However, time did not allow for further investigation.

Last-minute experiments were performed with again a different solvent to process ZnO: cyclopentanol. This dispersion is clear (the dispersion in acetone is milky). This indicates that there might not be large aggregates. It is then possible to print silver on top of this ZnO layer and it does not crack. However, to obtain good conductivity the required sintering time is much longer (5 minutes: > 10 kΩ, 20 minutes: ±80 Ω, 30 minutes: 20 Ω, 40 minutes: 9 Ω) than for silver on glass. Hence a thicker silver layer was applied (by setting drop spacing to 10 µm) that conducted well (1 Ω) after 20 minutes sintering. The devices worked as diodes, but not as solar cells: there was no photocurrent. It is also observed that the color of the active layer has changed when comparing with other devices, thus it might be that the PCBM is dissolved by the cyclopentanol. Because also the photoactive layer is changed these experiments do not prove that the aggregates are the origin of the cracks. However, both effects (no cracks and long sintering) are interesting for further research and indicate that the crack formation can be solved. However, this could not be done due to the deadline for this report.

4.3-II PRINTING OF SILVER ON PFN2

When it was discovered that also PFN worked well as an ETL with an evaporated cathode it was immediately tried in combination with a printed silver cathode. Initial experiments on glass with the first batch of PFN we had available (PFN2 obtained from 1-material) showed that wetting of the silver ink was good and that no cracks appeared on the silver. Best of all: the silver conducted and the solar cells worked. However, the performance was much lower than with an evaporated electrode (the best MPP of PFN2 with a printed cathode was 1.4 mW/cm^2 versus a best MPP of PFN2 with evaporated cathode of 2.5 mW/cm^2). Still the results were very promising.

A follow-up experiment was done to optimize the sintering time. Normally 20 minutes of sintering is applied to ensure good conduction of the silver. This is applied in an oven in air at 120°C. However, earlier I tried the effect of annealing in air versus annealing in N_2 for the *npZnO* design – that showed a drop in performance, which could be partially corrected by further annealing in nitrogen. Thus a series was made to compare different sintering methods. The sintering time in air was varied and before measurement the devices were annealed / sintered a further 10 minutes on a 130°C hotplate in nitrogen. After 3 to 5 minutes of sintering in air the silver has transformed from the wet and gray ink to a reflective silver surface. However, it was even possible to obtain working devices that were not sintered in air but only sintered in N_2. Figure 45 shows the effect of sintering time on photovoltaic performance. The differences are not big, but it clearly shows there is no need to sinter more than 5 minutes in air. Now the best MPP of PFN2 with a printed cathode was 1.9 mW/cm^2.

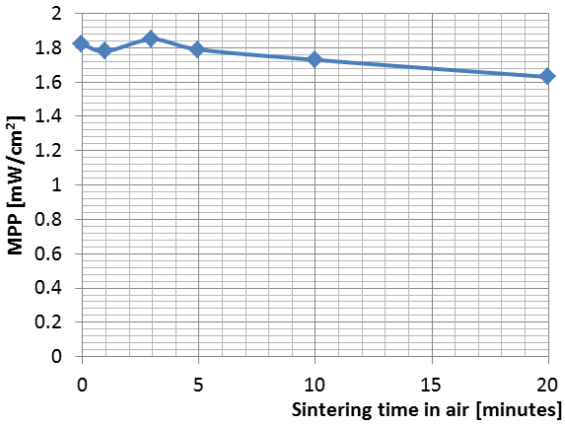

Figure 45 - MPP as a function of sintering time. The interlayer was PFN2. Before measurement (but after sintering) the devices were annealed for 10 minutes inside the glovebox.

The yield of working devices from this series was comparable to devices with an evaporated cathode. Out of the 40 produced cells on 10 devices there were 35 cells with a performance of more than 0.5 mW/cm^2.

4.3-III PRINTING OF SILVER ON PFN1: S-SHAPES

When it was discovered that PFN1 was more efficient than PFN2 with an evaporated electrode, also printing of silver on PFN1 was tried. The most obvious change when switching from PFN2 to PFN1 was the fact that the initial measurement showed S-shaped *J-V* curves (red in Figure 46) which were not observed for PFN2 cells. If the cell was left under simulated sunlight for ~5 minutes the S-shape decreased and the performance increased (blue). The same effect could be obtained by applying a pre-measurement UV-treatment (λ = 365 nm, ~5 minutes) and this has been applied for all other *PFN2* cells with a printed cathode. It is also noted that the S-shape returns after a while and the UV-treatment needs to be repeated.

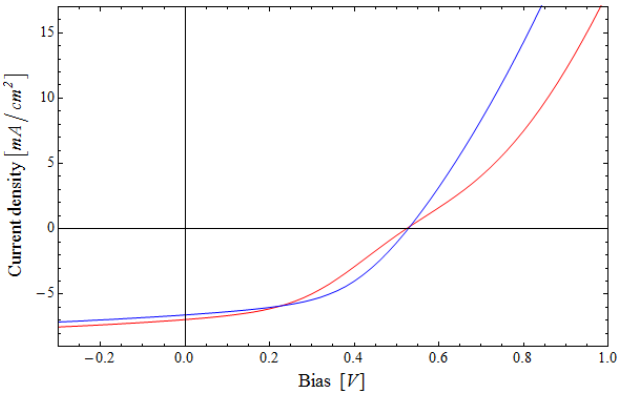

Figure 46 – PFN1 with printed cathode with has an S-shape (red). This is resolved by either leaving in in the simulated sunlight for ~5 minutes (blue) or by applying ~5 minutes of UV (λ = 365 nm) before measurement.

As indicated in section 2.4-I A) S-shapes often happen in the case of ZnO layers, and it is a known effect for metal oxides. There the UV-treatment helps because it increases the n-type doping in the ZnO layer and thus the number of mobile electrons by the desorption of oxygen. It is known that PFN also absorbs in the UV [65]. Results in section 4.4-IV show that the S-shape in these devices is also probably related to oxygen uptake. A possible hypothesis is that the oxygen might bind to the PFN by accepting free electrons, which causes the PFN layer to become insulating. The insulating effect than limits the charge transfer across the interface and causes the characteristic S-shapes (section 2.2-I B). It could also be that a silver oxide (Ag_2O) is formed which is solved by UV-illumination. Finally, there could be some effect of residual solvents used to process the device. These theories could not be investigated in the timeframe of the project.

4.4 ALL SOLUTION PROCESSED DEVICES

The next step after realization of the solution-processable cathode would be to show an all-solution processed device. To make this an inkjet-printed silver grid will be used as anode in combination with high-conduction PEDOT. From then on the stack will be the same. To wrap up the steps involved in the production of these devices: first a grid is printed by me, with on top of that high-conduction PEDOT:PSS printed by Harrie Gorter (section 3.2). Then the photoactive layer (PAL) is spincoated (section 3.3). After the photoactive layer has dried either PFN1 or PFN2 is spincoated on top (section 3.4-IV). Then the silver cathode is printed with the default settings (section 3.6-III). After sintering for five minutes the devices are transferred into the glovebox. In the glovebox the devices are annealed / sintered for another 10 minutes and then the measurements are performed. This production scheme will be used for the rest of this paragraph. A combination of options gives three possible different devices for both PFN1 and PFN2: "*PFN1/2 evaporated*" with an evaporated silver cathode, "*PFN1/2 printed*" with a printed silver cathode (both Table 3) and "*PFN1/2 ASP*" with both a bottom grid and a printed cathode (Figure 47).

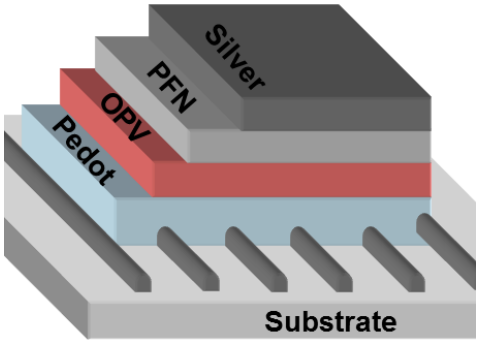

Figure 47 – The design of *PFN ASP*.

4.4-I PROBLEMS WITH THE ANODE

The printing of grids is a known process but it can be very complicated to obtain good grids. This is because the height of the grids should be as low as possible to avoid shunted devices. This means a high drop-spacing has to bee used, but this can cause the separate head-movement lines to be disconnected (Figure 48). However, if wetting is increased by an ethanol flushing step the wetting is too good and the ink is not pinned to the grid lines anymore: dendrimers appear (Figure 49). Without the ethanol flushing step approximately half of the grids looked reasonable "good".

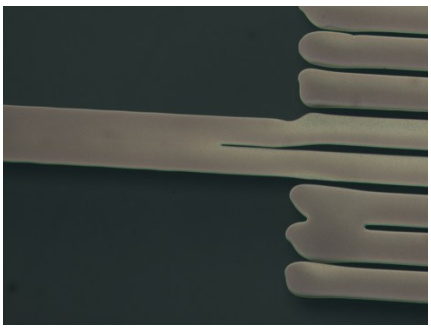
Figure 48 - Disconnected lines in printed grids

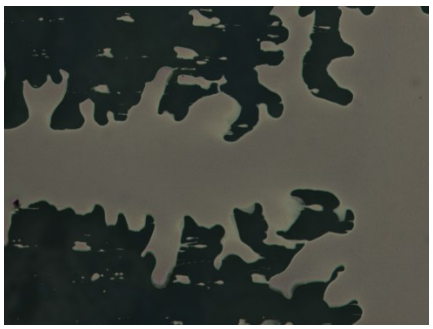
Figure 49 - Dendrimers

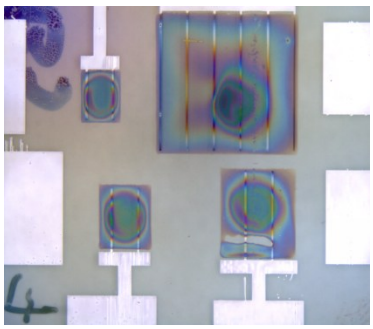
Figure 50 - HC-PEDOT on top of a grid

The next step of was the printing of the high-conducting PEDOT:PSS. Initially the thickness was set to ~100 nm, but the layers were not closed. Thus it was chosen to move to a higher thickness of ~200 nm: some light will be lost, but the risk for shunted devices will be lower. A typical grid with PEDOT can be seen in Figure 50. On the C-cell a dewetting spot can be seen, this is probably caused by incomplete cleaning or soap-rests on the surface. Also the color is not constant which means the thickness is not constant. This has allready been indicated in Figure 20.

4.4-II Results for *PFN2 ASP*

The first result for an all-solution processed cell was obtained with PFN2. The results are shown in Figure 51. Three measurements on the same device are shown. The first two measurements have been done before the annealing in the glovebox. The first measurement (red) showed a device with a large shunt. This is a known effect when using grids with high-conducting PEDOT:PSS and can be solved by using a negative bias treatment. When -20 V is applied to the cell for ~2 seconds the shunts will be "burned out" and the performance increases to the blue line (MPP ~0.6 mW/cm^2). However, as was already known from section 4.3-II, performance can be increased by an addition annealing / sintering in nitrogen (green line, MPP ~1.7 mW/cm^2). This annealing was thus done as standard on the rest of the devices and when necessary also a reverse bias treatment has been applied. On the four grid devices classified as "good" which were made as *PFN2 ASP* there were six cells with a performance of > 1.4 mW/cm^2 and some more with lower performances, but on all "good" grids at least one cell worked well. The yield is thus very low (6 out of 16), but this is mainly due to the bad quality of the printed grids and could be solved by using the Holst embedded grids. It must be said that later, for the *PFN1 ASP* devices the yield was 10 out of 12 for the good grids, which might be related to more experience with for example the shunt burning.

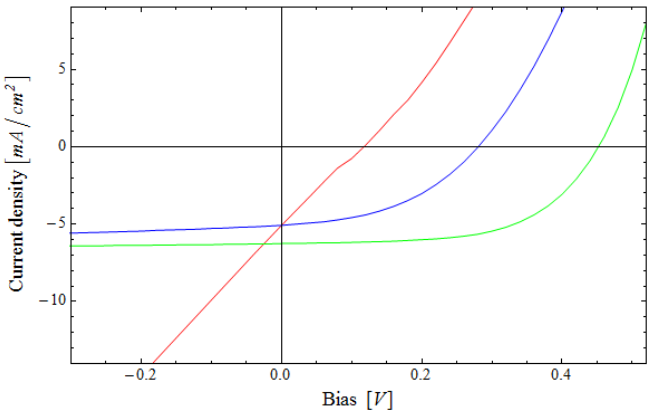

Figure 51 - three times the same cell on a *PFN2 ASP* device. Just after sintering without further annealing in the glovebox (red), after application of negative bias treatment to burn shunts (apply -20 V during 2 seconds) (blue) and after annealing in the glovebox for 10 minutes at 130°C (green).

4.4-III Results for PFN1: Direct Comparison of Evaporated, Printed and ASP

With the PFN1 a direct comparison has been made – the photoactive layer was processed from the same solution and on the same day for all three different structures: *PFN1 evaporated, PFN1 printed* and *PFN1 ASP*. These results can thus be directly compared. Two significant things can be seen in the representative plots shown in Figure 52 and Figure 53. The first is shown in Figure 52: when switching from an evaporated cathode to a printed cathode the maximum current density in forward bias decreases (blue arrow). This is caused by the increase in series resistance from 2.7±0.9 Ω to 4.3±1.3 Ω which is calculated from the inverse slope of the *J-V* curve between 1.5 and 2 Volt. This is an expected effect because it is known that printed silver inks have a higher resistance than evaporated silver. When the anode is replaced by a grid the current density in forward bias increases again to even higher levels than for the *PFN1 evaporated* device (green arrow). Also the series resistance decreases to 2.1±1.4 Ω. This is because the busbar of the grids has a lower resistance than the ITO electrode.

When looking at the short-circuit current density J_{sc} it seems to decrease by ~30% (Figure 53) when switching from an evaporated electrode to a printed cathode. Then the switch to a grid as anode does not cause the current density to decrease much further. This was not expected, because the grids and the thick high-conducting PEDOT block quite a lot of light. When we look at the current at -2 V however, the devices behave as expected. From *PFN1 evaporated* to *PFN1 printed* the current decreases by 18% (blue arrow in Figure 53) - this will probably be due the fact that a printed cathode will be less reflected. The difference in the current density between -2 V and 0 V can either be explained by the higher series resistance or by the fact that sintering has been done in air in the presence of the cathode (post-anneal) – when using an evaporated cathode it is known that annealing can be better done

before evaporation (pre-anneal), but this is off course not possible for a printed cathode that requires sintering. A sign that this could be the case is shown in the microscope images in Figure 54 and Figure 55 – large domains appear underneath the cathode. These large domains could cause problems for the extraction of charges and the bias-dependent photocurrent is a typical effect of that.

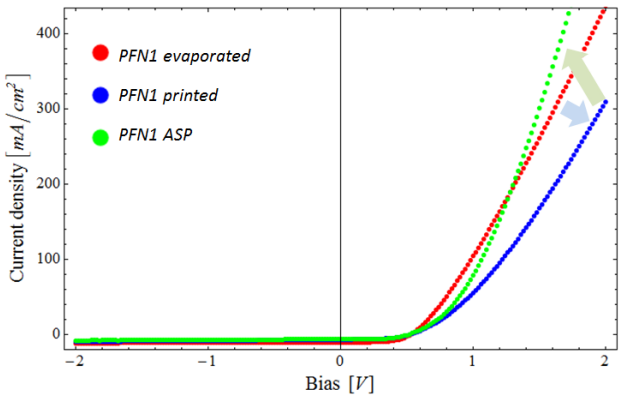

Figure 52 - Direct comparison for *PFN1* in positive bias

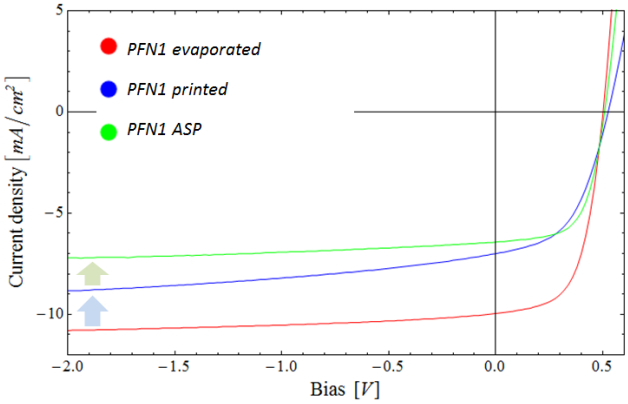

Figure 53 - Direct comparison for PFN1 in negative bias

The change from *PFN1 printed* to *PFN1 ASP* again causes a 18% decrease in current density at -2 V bias (green arrow in Figure 53). This can be explained by the fact the grids block some of the light. Also the high-conducting PEDOT is quite thick and thus transmits less light. However, these charges appear to be extracted without problems, because the J_{sc} for *PFN1 ASP* is only decreased by a small amount compared to the value at -2 V, even though the structures under the cathode in Figure 54 are also present in this case. There are two possible explanations: either the fact that the current density is initially lower decreases the charge extraction problems and/or the decreased series resistance allows charges to be extracted more easily – however, the series resistance on the cathode-side of the cell will still be the same, because the cathode is processed in the same way.

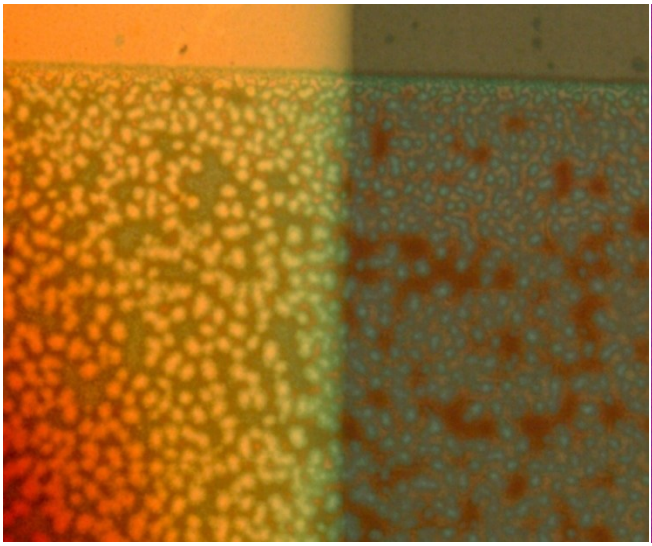

Figure 54 - microscope image looking through the cell to the bottom of the cathode (50x). On the left on top of PEDOT, on the right on glass.

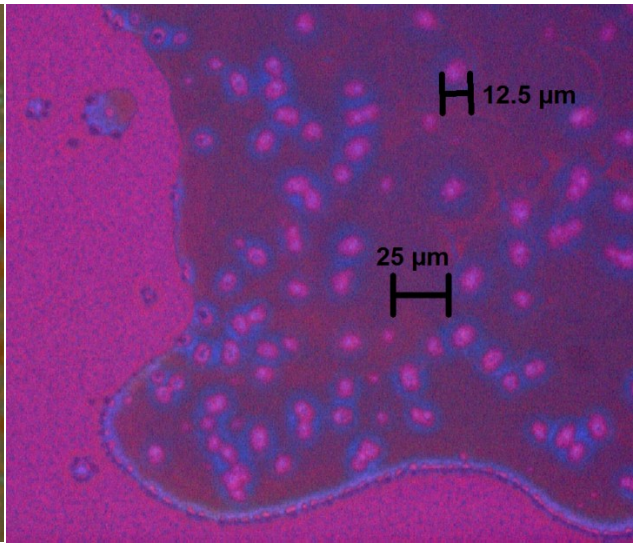

Figure 55 – same effect as Figure 54, but magnification 200x using different filters (color difference) and size of domains is indicated

Finally, because of the combination of the two effects the *PFN1 printed* and *PFN1 ASP* devices perform the same. The comparison for all devices made on the same day is shown in Table 6. The lower R_{shunt} for *PFN1 printed* is an effect of the problematic charge extraction. The best performing *PFN1 ASP* devices obtain a MPP of 2.0 mW/cm^2.

Table 6 – Average performance of *PFN1* devices. A reasonable selection has been made that excludes malfunctioning devices. The column 'based on' shows how many cells from how many devices are used in the average. The PAL of all devices was made on the same day from the same solution thus the current densities can be compared. R_{series} and R_{shunt} have been calculated from the inverse slope of the *J-V* curve around respectively 1.75 V and 0 V.

	Based on	J_{sc} [mA/cm^2]	V_{oc} [V]	FF [%]	MPP [mW/cm^2]	R_{series} [Ω]	R_{shunt} [Ω]
PFN1 evaporated	3|2	10.3 ± 0.5	0.51 ± 0.02	58 ± 3	3.03 ± 0.35	2.7 ± 0.9	775 ± 120
PFN1 printed	4|2	7.0 ± 0.1	0.52 ± 0.01	51 ± 1	1.85 ± 0.06	4.3 ± 1.3	477 ± 19
PFN1 ASP	14|6	6.6 ± 0.4	0.51 ± 0.01	55 ± 5	1.86 ± 0.14	2.1 ± 1.4	740 ± 380

A series has also been measured using the EQE setup at TU/e to verify the accuracy of the calibration at TNO. For each type two cells on one device has been measured. The EQE has been used with and without bias, but the results are shown without bias – this is because the values were lower without bias and there were some problems with the bias-adjustment, so this is done to make sure we are not overrating the devices. The expected current density is calculated by combining the EQE results with the AM1.5 solar spectrum. When this is combined with the V_{oc} and the FF the expected power conversion efficiency η can be calculated. The results are shown in Table 7 and show that the difference between the two methods is small, except for *PFN1 ASP C*, for which there appeared to be some degradation in between the measurements. The results however confirm all-solution processed devices can be made with an efficiency close to 2 %. It should be noted that the EQE measurement is done on a small spot on the cell area. The non-uniform PEDOT thickness for the *PFN1 ASP* cells could cause deviations because less light will enter the cell through thicker areas. This was not accounted for in the measurements.

Table 7 - Results from EQE measurements compared with measurements at TNO

	TNO J_{sc} [mA/cm^2]	*EQE* J_{sc} [mA/cm^2]	V_{oc} [V]	FF [%]	MPP TNO [mW/cm^2]	η from EQE [%]
PFN1 evaporated A	9.7	10.07	0.476	55.7	2.56	2.67
PFN1 evaporated C	10.7	10.87	0.520	52.2	2.91	2.95
PFN1 printed A	7.0	6.90	0.520	50.0	1.82	1.79
PFN1 printed C	7.2	6.99	0.515	45.0	1.67	1.62
PFN1 ASP A	6.4	6.21	0.502	62.7	2.01	1.95
PFN1 ASP C	7.0	5.93	0.509	54.6	1.96	1.65

4.4-IV Results for PFN1: Initial Stability

Because of the success of the all solution-processed devices it will be interesting to see the stability of these structures with respect to oxygen, temperature and light. The degradation should be limited before a decision is made to upscale the production of these devices. At Holst Centre no setup is available to reliably test stability (like for example at DTU [63,83,84]. However, it is possible to obtain an initial estimate. Three different methods were tried: 64 hours in air in the dark, 64 hours at 85°C in N_2 in the dark and 16 hours under simulated sunlight conditions in N_2 (temperature will be ~50°C because of light-induced heating). The heat treatment had no significant effect. The effects of the other two methods are discussed are discussed in this section.

After storage in air for 64 hours in the dark the performance significantly degraded due to a large S-shape (red in Figure 56). This could however be largely reversed by keeping the devices for ~15 minutes under simulated sunlight conditions in N_2 (blue). The performance reached almost the same level as before the exposure to air (green). If watched closely it is possible to still see a small S-shape in the blue curve, thus perhaps the UV-treatment was not long enough. The fact that the S-shape is much more severe for a sample stored in air than a sample stored in nitrogen indicates that the S-shape is related to oxygen uptake. See also section 4.3-III.

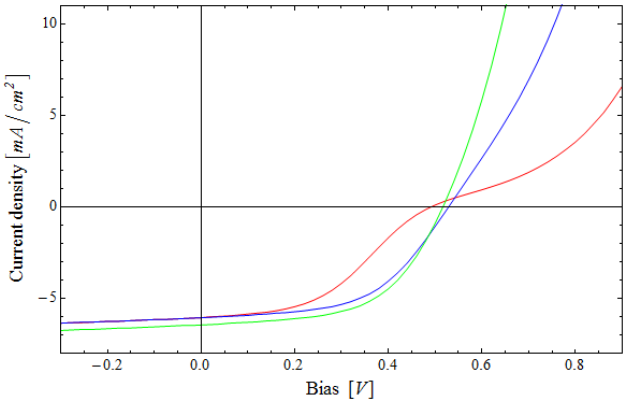

Figure 56 - *PFN1 ASP* device before (green) 64 hours in air (in the dark), directly after (red) and after ~15 minutes simulated sunlight conditions (blue)

The effect of exposure to sunlight has been investigated by exposing a *PFN1 ASP* device to simulated sunlight in the *J-V* measurement setup for 16 hours. The results can be seen in Figure 57. The blue line is before the exposure. After exposure, the series resistance (as estimated from the slope at high bias) decreased from 1.31 Ω to 0.94 Ω. This is probably because the pre-exposure measurement was still a bit S-shaped, which has been completely removed by the UV-exposure during the 16 hours. The seconds effect is the decreases photocurrent as seen in J_{sc}. Because the V_{oc} has not significantly degraded this degradation is expected not to be caused by the PFN but by the photoactive layer itself. The MPP decreased from 1.8 to 1.5 mW/cm^2.

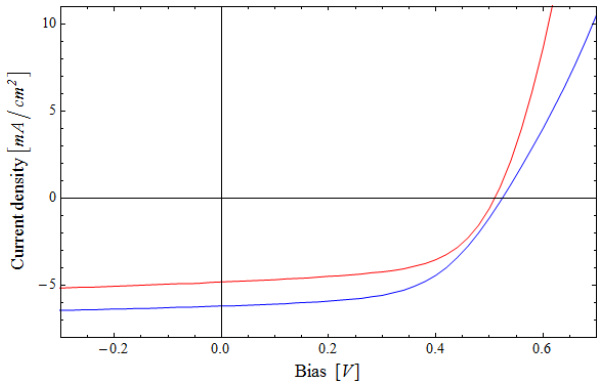

Figure 57 - *PFN1 ASP* device before (blue) and after (red) 16 hours of exposure to simulated sunlight.

These initial stability tests do not indicate any significant problems. To be sure about the stability it would be good to include these cells in a more extensive stability study.

4.5 CORRELATION PLOTS

The database system makes it possible to compare large amounts of data. For example, the relation between cell area and performance can be studied. Figure 58 shows that the fill factor decreases for increasing cell area, caused by both an increase in series resistance and a decrease in shunt resistance for the larger cells. Each point in a graph is the result of a complete *J-V* measurement. All measurements done when plotting these graphs which showed an efficiency of more than 1.5% are included in these plots (364). This is done to avoid wrong determinations from shorted devices or measurement errors.

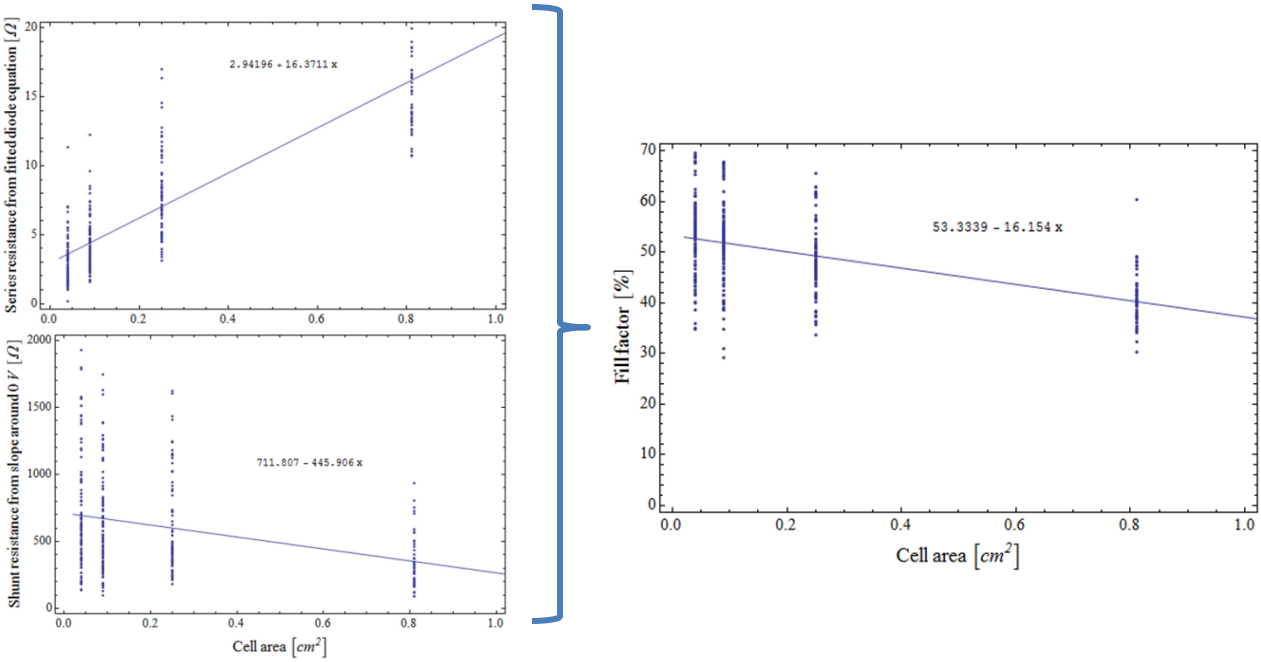

Figure 58- Decreasing fill factor caused by increasing series resistance and decreasing shunt resistance for larger cell areas

It also interesting to verify the validity of the various estimation methods of diode parameters. For example, the inverse slope around 2 V (*slope2V,* as explained in section 2.2-II A) can be used to estimate the series resistance. The series resistance can also be determined by fitting the diode equation to the obtained data (*lightRs*, as explained in section 2.2-II C). Ideally they should be the same. This can be verified by plotting *slope2V* on the y-axis versus *lightRs* plotted on the x-axis. The slope of that plot should be 1. It is shown in Figure 59 that the slope is 1.06, thus the estimate is fairly good.

However, as shown in Figure 60, the relation is not consistent for the estimate of the shunt resistance from the inverse slope around 0 V (*slopeRsh*) and the value obtained from the fitted diode equation (*lightRsh*). This discrepancy can be explained by the fact that the photocurrent in organic solar cells is often bias-dependent (enhanced extraction of charges in electric field), which is not included in the single diode model. Because of this the apparent shunt resistance actually consists of multiple parts: the “real” shunts and bias-dependent photocurrent. This effect is handled differently by both estimations.

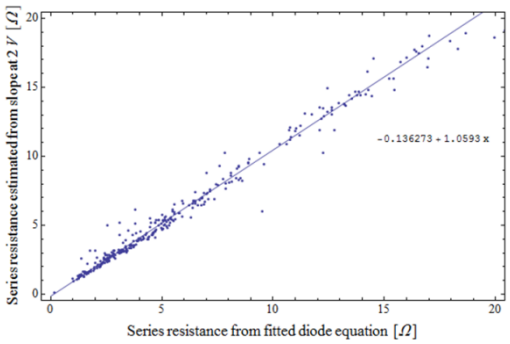

Figure 59 - Relation between *lightRs* and *slope2V.*

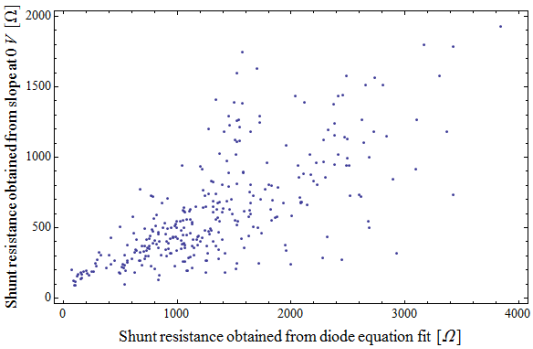

Figure 60 - Relation between *slopeRsh* and *lightRsh.*

Finally it is shown in Figure 61 that the database system makes it possible to show a lot of results in a convenient and easily understandable format. The figure shows the open circuit voltage of all measured devices of the structures *reference, onlyAg, Znacac, npZnO, npZnO|MUA, PFN* and *TiOx* as are introduced in section 2.4-I. The *reference* devices always have a V_{oc} between 0.50 and 0.55V. When the LiF|Al cathode is replaced by only an evaporated silver cathode, the V_{oc} immediately drops to around 0.40V. The addition of an ETL/HBL (more on this in section 4.1) shows that the V_{oc} increases to ~0.50V again, except for the *TiOx* devices where we were not able to show the desired effect. It also shows a large spread in the data for the ETLs: this is due to reproducibility issues.

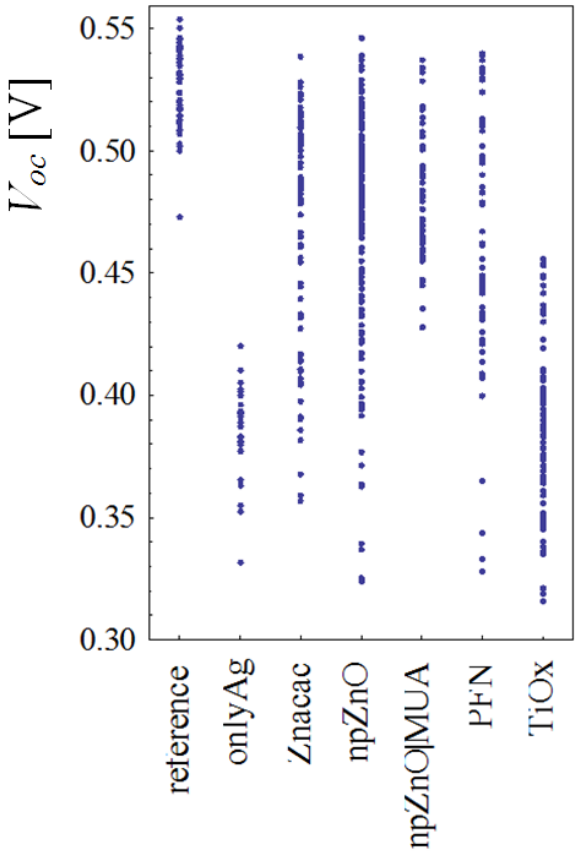

Figure 61 - Cell structure *versus* open circuit voltage

5 CONCLUSION

The comparison between the 'reference' design (with a LiF aluminum cathode) and devices with an electron transport layers in combination with an evaporated silver cathode show that the latter can also be used as a cathode in organic solar cells with a relatively small loss in performance (~12%). This showed that it is possible to develop a solution-processable cathode in which the silver will be inkjet-printed instead of evaporated.

These devices with printed silver cathodes have been made. For one of the electron transport layers, ZnO, it was not possible to obtain reliably working devices because of crack formation. A lot of effort has been put in the prevention of these cracks but this did not succeed. Two possible hypothesis have been given that could explain the crack formation, but it could not be solved in the timeframe of this project. However, a different electron transport layer, PFN, showed that the principle was working: devices were produced reliably with over 50% of the efficiency of the reference design.

The good results for the combination of a PFN interlayer with printed silver showed that it should be possible to make all-solution processed devices and these have indeed been made. Photovoltaic conversion efficiencies up to almost 2.0% have been reached – this is about 40% lower than the reference design. The losses have been reasonably explained and originate from less reflection, sintering in air, post-annealing instead of pre-annealing and shadowing effects from the grid and thick high-conducting PEDOT. Initial device stability tests do not show any big problems but this should be investigated further.

It is interesting to note that PFN also works with higher efficiency materials like PTB7 [67]. It is expected that these all-solution processed solar cells can also be made using these photoactive layer materials. However, the requirement for sintering can be a problem for higher efficiency materials, because the new materials often do not survive temperatures above 80-100°C. Ongoing research in silver inks and other sintering methods like photonic flash sintering could mediate this problem. This means that high-efficiency solar cells produced by printing and coating on a roll-to-roll basis are certainly feasible.

6 APPENDIXES

6.1 SURFACE CHARACTERIZATION USING CONTACT ANGLE MEASUREMENTS

The organic solar cell always consists of multiple layers. In a roll-to-roll compatible process these layers all have to be processed using a solution. The deposition of a layer from solution on top of a surface is a highly complicated process. To name a few factors that influence the new layer: topology of the surface, the polarity of the surface, the total surface energy, the surface tension of the solution, the wet layer thickness and the solvent evaporation speed. To gain insight in some of these surface properties contact angle measurements have been employed.

In 1805 Young discovered that there is a relation between surface tensions and the contact angle of a drop on a surface [85]. Equation (VII) is derived from the equilibrium of forces [86,87] as shown in Figure 62.

$$\text{(VII)} \qquad \sigma_s = \sigma_{ls} + \sigma_l \cos\theta$$

Here σ_s is the surface tension between the solid and the gas, σ_{ls} is the interfacial tension between liquid and solid and σ_l is the surface tension between the liquid and the gas. The contact angle can be measured with a camera-setup shown in Figure 63. Often the surface tension of the liquid is known but the other two are not. We are interested in the surface energy of the solid.

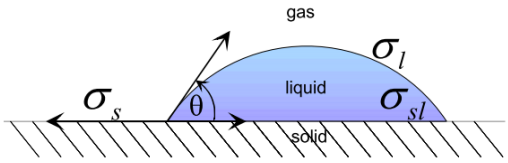

Figure 62 - Drop on surface. Image taken from [86].

Figure 63 - Easydrop available at Holst Centre [88]

The simple approach shown above cannot be the whole story. The forces between the liquid and solid are not always of the same type. We distinguish “polar” (ionic bonds, hydrogen bonds, acid-base interactions) and non-polar (van der Waals) or “disperse” forces. Because of this the surface tension of the liquid and the surface energy of the solid consist of two parts:

$$\text{(VIII)} \qquad \sigma_s = \sigma_s^d + \sigma_s^p \qquad \& \qquad \sigma_l = \sigma_l^d + \sigma_l^p$$

According to Owens, Wendt, Rabel and Kaeble (OWRK) [89] the interfacial energy between solid and liquid can be calculated according to the geometric mean:

$$\text{(IX)} \qquad \sigma_{ls} = \sigma_l + \sigma_s - 2\left(\sqrt{\sigma_l^d\,\sigma_s^d} + \sqrt{\sigma_l^p\,\sigma_s^p}\right)$$

If equation (IX) is substituted in equation (VII) and some rewriting is done it gives a straight line for the cosine of the contact angle as a function of the surface tension components of the liquid (see [86]). The polar part of the surface energy can be calculated from the slope and the disperse part can be calculated from the intersect with the vertical axis. Thus if the contact angles for a few liquids with different polar parts are measured an estimate can be given for the surface energy of the solid.

There are more methods to estimate the surface energy, for example the method according to Wu, the method according to Fowkes or using acid-base interaction. However, OWRK is a commonly used method and gives satisfying results.

Once the polar and disperse parts of the surface energy are known it is possible to calculate all combinations of polar and disperse parts of liquid surface tensions which would give a contact angle of 0°. A plot of this is called a wetting envelope [90]. Liquids that fall "in" this envelop will wet the surface but liquids that fall outside the envelop will only wet partially. This knowledge is very useful when searching for solvents that can be used on top of the photoactive layer or cathode modification layer.

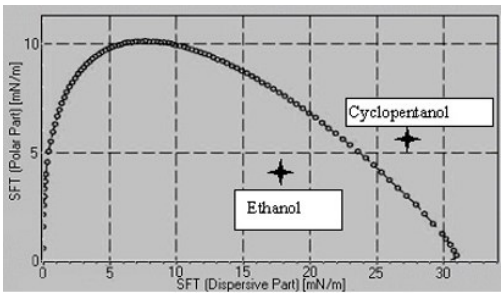

Figure 64 - Wetting envelope (image taken from [90])

6.2 DATABASE INTERFACE

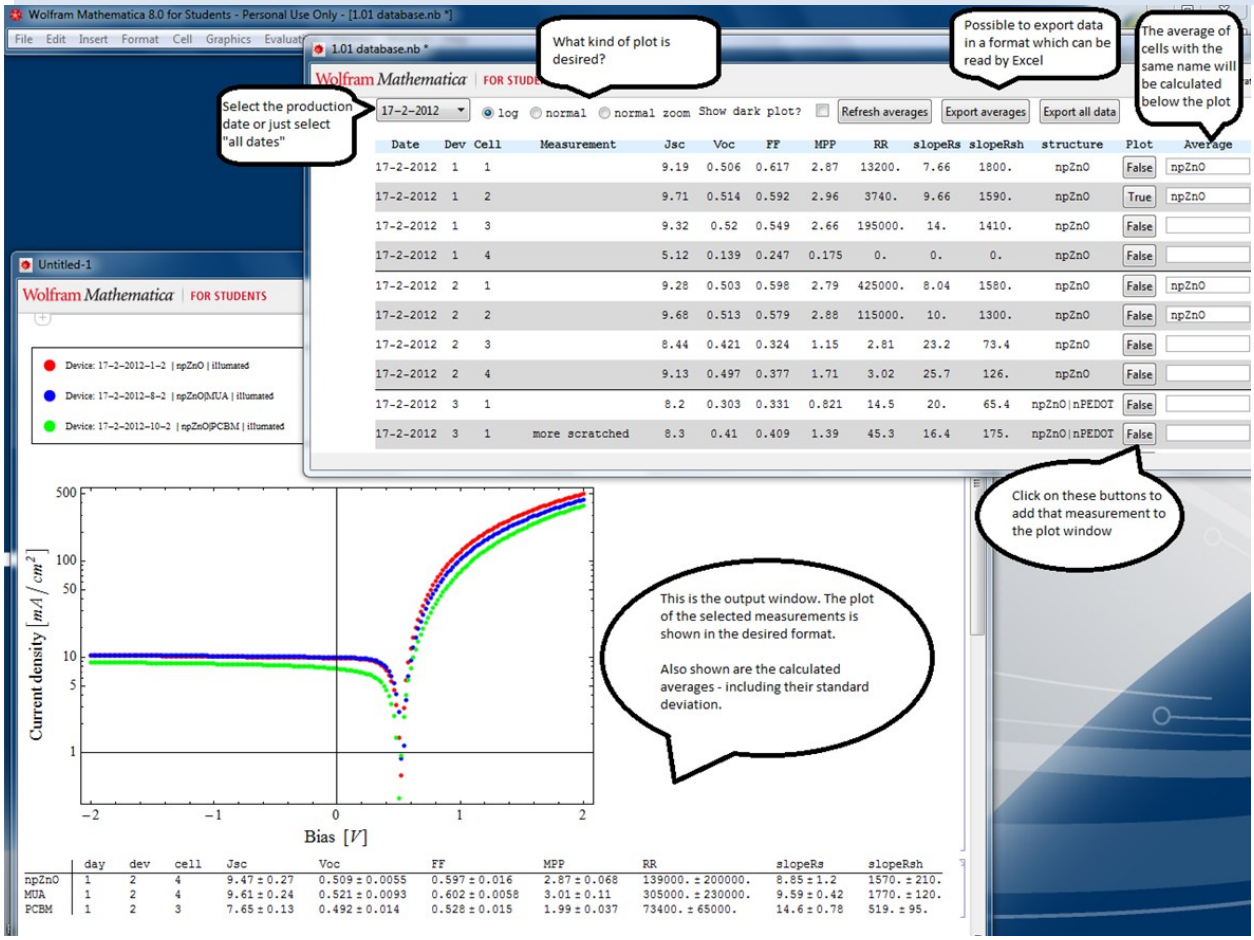

Figure 65 - Interface for database system in Mathematica

6.3 GRADUATION RESEARCH PROPOSAL

This is the original research proposal which was written and signed in December 2011

6.3-I PROBLEM DEFINITION

At the Holst Centre the aim is to develop organic solar cells that can be made entirely (including electrodes) by printing and coating. A lot of work has been done on the anode, however the solution processing of the cathode (in conventional device architecture) still forms a problem. A potential cathode architecture includes a zinc oxide (ZnO) electron transport layer with a silver electrode on top of that. However, the printing of silver on top of ZnO has wetting problems – therefore the aim is to include a PEDOT:PSS layer between the ZnO and silver – however, a less-acidic kind of PEDOT:PSS has to be used to be able to print it on top of ZnO. Some work has been done on this already at the Holst Centre, but the results were ambiguous. The exact question is if the device architecture as proposed above is a viable architecture to make an all-solution processable cathode. Sub-questions are to investigate the loss-factors that will be involved and how to minimize these losses by optimizing processing conditions. If time allows it will also be tried to show a device processed entirely from solution.

6.3-II SCIENTIFIC AND SUSTAINABLE ENERGY TECHNOLOGICAL RELEVANCE

Solution-processing offers large advantages over other thin-film deposition techniques. It can be applied to large substrates in large volumes. If entire solar cells can be produced by a solution process it will be possible to use a roll-to-roll process to print and coat solar cells. This enables the production of cheap and flexible solar cells.

Scientifically the interface effects are very interesting. The workfunction of the contacts is generally acknowledged to be of vital importance – how is this affected by the quality of the ZnO layer? What influence do the processing parameters have and what causes this (e.g. interface dipoles)? How can we ensure good wetting (necessary for a closed layer) without affecting the photoactive layer?

6.3-III METHOD

Because everything happens at the nanoscale it is difficult to be sure why some effect is measured — a decreased efficiency can be caused by many factors. Therefore the development of a new cathode is a step-by-step process. First reference cells using the conventional structure ITO | PEDOT:PSS | P3HT:PCBM | LiF | Al are made. Then two possible methods for the ZnO layer are investigated (precursor or nanoparticles). These can be deposited on the photoactive layer and will be tested with an evaporated silver electrode. It this set-up the processing of the ZnO layer can be optimized. Then the PEDOT:PSS layer is included, still using the evaporated silver electrode. In this way the processing of the PEDOT:PSS layer can be optimized. Finally the silver electrode will be printed instead of evaporated.

Characterization will mainly be done by current-voltage measurements under simulated sunlight and layers will be investigated using optical microscope and a profilometer. When required more elaborate techniques may be used.

6.4 WORK REPORT

This section will give additional insight in the step-by-step progress which has been done in this graduation project.

6.4-I EARLIER WORK

Before starting the project my supervisor Yulia Galagan and a student (Jo van Gorp) had already worked on the printed cathode. It had been tried to print silver directly on a ZnO layer prepared from $Zn(acac)_2$ but this didn't work. Then cells were prepared using a PEDOT layer to allow for the printing. However, the results were ambiguous. Devices all performed bad, but reference devices didn't work well either.

6.4-II DECEMBER 2011

While settling in the new company environment a literature study was done to gain more insight in the project at hand. General information about the (charge extraction) processes in organic solar cells, detailed reports about (hole blocking) ZnO layers and the additional PEDOT layer as used in tandem cells. Also information has been found about the conversion of $Zn(acac)_2$ into ZnO and about the wetting behavior of PEDOT layers.

Also important in this period was to acquire instruction for the chemical lab and the cleanrooms. After this had been done it was possible to start producing reference devices with a LiF | Al cathode, which performed as expected.

After this had been done it was time to start looking into the ZnO layer, because there were doubts about the $Zn(acac)_2$ conversion – is the layer really ZnO? Different deposition (hot/cold) or annealing (pre/post and direct/after 30m) methods were tried using an evaporated silver cathode. Cells were performing better than without the ZnO layer, but performance varied widely. This could be explained by microscope images showing 'drops'. These results could explain the inconsistent results acquired earlier.

6.4-III JANUARY 2012

The problems involved in the deposition of a neat layer made us move towards other solvents. Work has been done by another Holst employee (Nadia Grossiord) and it has been shown that it is possible to prepare a neat layer of $Zn(acac)_2$ using pentanol instead of ethanol. Also a nanoparticle ZnO solution was tried. Both the layer deposited from pentanol and the nanoparticle solution gave far more consistent results. The nanoparticles performed better than the (probably) incompletely converted $Zn(acac)_2$. However, both were used for the further process because the layers might have very different properties.

Then the neutral PEDOT which was found to be the best in previous research was tried on top of these layers. It was immediately clear that wetting behavior was not ideal and a lot of cells were shorted or underperforming. Because of the inconsistencies in the preceding research the different PEDOTs were investigated again. To gain insight in the wetting behavior contact angle measurements were done for all PEDOTs on both layers. All PEDOTs were again used in devices but most were underperforming again. The one which functioned best corresponded to the one found in the previous research. To check reproducibility four devices for both the np-ZnO and $Zn(acac)_2$ layer were made. PEDOT deposition was now under control – and all devices were shorted while the devices without PEDOT performed as expected. This bad news had to be investigated using thermography to gain insight in

the cause of the shorts, because it could have been related to the scratching of the (high conducting) PEDOT or to the whole area. The latter was found to be the case, thus these PEDOTs are not suitable for our purpose.

6.4-IV FEBRUARY 2012

Having found that the PEDOTs were not suitable there was time without experiments in which I decided to investigate the *JV* behavior of the solar cells, because I observed a large decrease in dark current in when adding the ZnO layer. It was desired to express this in numbers. While reading about *JV*-modeling and trying to fit diode parameters it was found that it would be convenient to have a database system, which I set up.

In the end of January I was introduced to both Jan Gilot and Pim Voorthuijzen who have been working in the same area. Jan had produced working and reproducible tandem devices at the TU/e, but was not able to repeat this here. The problem was the same as I had and related to the PEDOT layer. He is testing PEDOTs in collaboration with Agfa and it was decided to avoid double work. Pim produces the ZnO nanoparticles and is working on a sol-gel method to prepare a TiO_2 layer which should have the same properties. This was also tried in our layer stack – results were promising but work still needs to be done, however the option has to be kept in mind.

Because of the problems involved in the PEDOT layer I decided to take a step back: why was it not possible to print silver directly on the ZnO layer? In previous research the wetting was 'too good' and the ink spread too much. After obtaining the inkjet printer instructions I however had very different results: wetting was excellent on both the $Zn(acac)_2$ layer and the nanoparticle ZnO layer. Devices with the $Zn(acac)_2$ layer were all shorted, but the np-ZnO devices did not conduct at all. Microscope images showed this was caused by cracks in the silver layer and one (albeit badly) working cell was produced by smearing silver paste on top of the silver ink.

These promising results demanded further investigation. The cracking of a layer is caused by stress, either due to point defects, interactions with the surface below, too fast drying or evaporation of solvent from underneath an already dry silver layer. Various strategies were employed to slow the drying which did have no effect. Also the 'double' application of a silver layer did not conduct. However, the addition of a monolayer of mercaptoundecanoic acid (MUA) on top of the np-ZnO layer seemed to have an effect, resulting in less cracks and some conduction. Sadly, the resistance was still too high for working devices.

6.4-V MARCH 2012

Still the options were not exhausted. Various different commercial silver inks are available. The one used before is supposed to work best in a wide variety of situations, however apparently not in this case. So, other inks have been tried. A systematic matrix has been set up (8 different inks, 5 different surfaces) to check if they were able to dry without cracking and thus conduct. A few promising inks have been selected and tried, but these gave shorted devices (more on this in April).

Also, some loose ends were looked in to. We observed significant degradation after one week in the glovebox, so a larger batch has been prepared which has been measured over time – this showed only a small performance decrease in dark storage. Also the effect of annealing in air has been studied, because sintering of silver ink is done in air. Then contact problems which lead to some photocurrent showing up in reverse bias and no current at all in forward bias were explained and solved. Finally, some effort has been taken to summarize some data, from which for example a day-to-day performance variation emerged. The summarized data was used in the mid-term presentation and to present some results in the Solliance meeting, which lead to interesting ideas and contacts.

6.4-VI APRIL 2012

The promising inks did not live up to the expectations. Thermography has been applied to investigate the cause of shorted devices. It appears to be point defects, but lots of them. If this is already giving so much trouble on the small scale in a cleanroom, how can it ever work on large scale? Now essentially two options remained:

- Use a different ETL/HBL instead of ZnO
- Investigate the cause of cracking and solve that problem

It was not possible to decide which of these would be the most promising, so they have both been tried. As a different ETL/HBL a couple of options were available: TiOx from our Solliance partner IMEC, the polymer PFN [66], Cs_2CO_3 [15,63] as ETL and it has been tried to obtain a SAM of hexadecanethiol that would lower the workfunction of silver [91]. They have all been tried with an evaporated silver layer. The last two didn't improve results over the case without the layer. PFN increases performance, but not as much as ZnO, however, silver printing has been tested on glass plates on top of PFN and works. TiOx works perfectly at IMEC, but in our lab it is not able to increase performance. This is being investigated. However, it is also possible to print silver on this.

To investigate the cause of cracking SEM and cross-sectional TEM have been made, which showed that the surface was not fully covered by ZnO. This was explained by instability of the ZnO nanoparticles in isopropanol, so we obtained a new batch in acetone. The increased performance suggests that we now have a good layer, but still cracks arise when printing silver. It was also observed that the silver was much thicker than expected. Using a smaller silver content it was possible to decrease the thickness. These two things combined gave layer that did not crack, however, it still did not conduct. Still, two devices were made that showed a 0.5% efficiency using lines printed twice (grid-structure) that did not crack and did conduct – not good, but it shows that if the cracks can be solved it should be working.

6.4-VII MAY 2012

Quite some effort was put into the IMEC TiOx – it is known to work but we can't get it to work. However, we were not able to fix the dewetting problems. More success was achieved with PFN – the first batch was used in cells with a printed cathode and worked with efficiencies up to ~2% compared with the ~2.5% reference. Then a new batch (synthesized by Koen Hendriks (TU/e)) even showed better performance in the reference design (~3%), however when combined with printed silver also the performance decreased to ~2%. Then it was shown that both PFNs could be combined with the Holst solution-processed anode (grid + HC-PEDOT) and thus create an all-solution processed cell with an efficiency of also ~2%.

Also some more work has been put in the explanation of the crack-formation on top of ZnO nanoparticles. SEM and AFM were performed and on the non-conducting silver even a conductive AFM was done. It is however still not possible to obtain a solid explanation.

6.4-VIII JUNE 2012

The final month was mainly spent on the writing of this report and the preparation of the final presentation. Also some additional measurements were performed on the ASP devices and some more AFM images were as comparison. Also a start has been made in the writing of an article about the results of this project.

7 BIBLIOGRAPHY

[1] R.A. Kerr, Energy supplies. Peak oil production may already be here., Science (New York, N.Y.). 331 (2011) 1510-1.

[2] International Energy Agency, World Energy Outlook 2011, OECD Publishing, 2011.

[3] J. Murray, D. King, Climate policy: Oil's tipping point has passed., Nature. 481 (2012) 433-5.

[4] T. Jianjun, Coal Mining Safety : China's Achilles' Heel, in: n.d. pp. 36-53.

[5] M. Yushi, S. Hong, Y. Fuqiang, The True Cost of Coal, n.d.

[6] N.S. Lewis, D.G. Nocera, Powering the planet: chemical challenges in solar energy utilization., Proceedings of the National Academy of Sciences of the United States of America. 103 (2006) 15729-35.

[7] A.. Becquerel, Recherches sur les effets de la radiation chimique de la lumiere solaire au moyen des courants electriques, Comptes Rendus De L´Academie Des Sciences. 9 (1839) 145-149.

[8] M. a Green, Photovoltaic principles, Physica E: Low-dimensional Systems and Nanostructures. 14 (2002) 11-17.

[9] C. Breyer, A. Gerlach, D. Schafer, J. Schmid, Fuel-parity: New very large and sustainable market segments for PV systems, in: 2010 IEEE International Energy Conference, IEEE, 2010: pp. 406-411.

[10] S.-I. Na, S.-S. Kim, J. Jo, D.-Y. Kim, Efficient and Flexible ITO-Free Organic Solar Cells Using Highly Conductive Polymer Anodes, Advanced Materials. 20 (2008) 4061-4067.

[11] D.-S. Leem, A. Edwards, M. Faist, J. Nelson, D.D.C. Bradley, J.C. de Mello, Efficient organic solar cells with solution-processed silver nanowire electrodes., Advanced Materials (Deerfield Beach, Fla.). 23 (2011) 4371-5.

[12] S.H. Eom, S. Senthilarasu, P. Uthirakumar, C.-H. Hong, Y.-S. Lee, J. Lim, et al., Preparation and characterization of nano-scale ZnO as a buffer layer for inkjet printing of silver cathode in polymer solar cells, Solar Energy Materials and Solar Cells. 92 (2008) 564-570.

[13] F.C. Krebs, Roll-to-roll fabrication of monolithic large-area polymer solar cells free from indium-tin-oxide, Solar Energy Materials and Solar Cells. 93 (2009) 1636-1641.

[14] S. Veenstra, F. Furthner, N. Grossiord, Y. Galagan, R. Andriessen, P. Blom, et al., Realization of an efficient, all solution processed polymer solar cell, in: n.d.

[15] W. Gaynor, J.-Y. Lee, P. Peumans, Fully solution-processed organic solar cells on metal foil substrates, Proceedings of SPIE. 7416 (2009) 741614-741614-7.

[16] C.J. Brabec, J.R. Durrant, Solution-Processed Organic Solar Cells, MRS Bulletin. 33 (2011) 670-675.

[17] Y. Galagan, J.-E. J.M. Rubingh, R. Andriessen, C.-C. Fan, P. W.M. Blom, S. C. Veenstra, et al., ITO-free flexible organic solar cells with printed current collecting grids, Solar Energy Materials and Solar Cells. 95 (2011) 1339-1343.

[18] Y. Galagan, B. Zimmermann, E.W.C. Coenen, M. Jørgensen, D.M. Tanenbaum, F.C. Krebs, et al., Current Collecting Grids for ITO-Free Solar Cells, Advanced Energy Materials. (2011) n/a-n/a.

[19] R. Abbel, J. van den Boomen, T. van Lammeren, T. de Koning, J.J.P. Valeton, E.R. Meinders, Current Collecting Grids for R2R Processed Organic Solar Cells, MRS Proceedings. 1323 (2011).

[20] E. Tekin, P.J. Smith, U.S. Schubert, Inkjet printing as a deposition and patterning tool for polymers and inorganic particles, Soft Matter. 4 (2008) 703.

[21] F.C. Krebs, Polymer solar cell modules prepared using roll-to-roll methods: Knife-over-edge coating, slot-die coating and screen printing, Solar Energy Materials and Solar Cells. 93 (2009) 465-475.

[22] M.S. White, D.C. Olson, S.E. Shaheen, N. Kopidakis, D.S. Ginley, Inverted bulk-heterojunction organic photovoltaic device using a solution-derived ZnO underlayer, Applied Physics Letters. 89 (2006) 143517.

[23] R.A.J. Janssen, Introduction to polymer solar cells, (n.d.).

[24] C. Deibel, V. Dyakonov, C.J. Brabec, Organic Bulk-Heterojunction Solar Cells, IEEE Journal of Selected Topics in Quantum Electronics. 16 (2010) 1517-1527.

[25] C.W. Tang, Two-layer organic photovoltaic cell, Applied Physics Letters. 48 (1986) 183.

[26] B. a. Gregg, M.C. Hanna, Comparing organic to inorganic photovoltaic cells: Theory, experiment, and simulation, Journal of Applied Physics. 93 (2003) 3605.

[27] N.S. Sariciftci, A.J. Heeger, Conjugated Polymer-Acceptor Heterojunctions; Diodes, Photodiodes, and Photovoltaic Cells, U.S. Patent 5331183-, 1994.

[28] P.P. Boix, J. Ajuria, I. Etxebarria, R. Pacios, J. Bisquert, Role of ZnO Electron-Selective Layers in Regular and Inverted Bulk Heterojunction Solar Cells, (2011) 407-411.

[29] S.E. Shaheen, G.E. Jabbour, M.M. Morrell, Y. Kawabe, B. Kippelen, N. Peyghambarian, et al., Bright blue organic light-emitting diode with improved color purity using a LiF/Al cathode, Journal of Applied Physics. 84 (1998) 2324.

[30] C. Waldauf, M.C. Scharber, P. Schilinsky, J. a. Hauch, C.J. Brabec, Physics of organic bulk heterojunction devices for photovoltaic applications, Journal of Applied Physics. 99 (2006) 104503.

[31] C.J. Brabec, S.E. Shaheen, C. Winder, N.S. Sariciftci, P. Denk, Effect of LiF / metal electrodes on the performance of plastic solar cells Effect of LiF, 1288 (2002).

[32] L.-M. Chen, Z. Xu, Z. Hong, Y. Yang, Interface investigation and engineering – achieving high performance polymer photovoltaic devices, Journal of Materials Chemistry. 20 (2010) 2575.

[33] M.R. Lilliedal, A.J. Medford, M.V. Madsen, K. Norrman, F.C. Krebs, The effect of post-processing treatments on inflection points in current–voltage curves of roll-to-roll processed polymer photovoltaics, Solar Energy Materials and Solar Cells. 94 (2010) 2018-2031.

[34] A. Wagenpfahl, D. Rauh, M. Binder, C. Deibel, V. Dyakonov, S-shaped current-voltage characteristics of organic solar devices, Physical Review B. 82 (2010).

[35] D.J.D. Moet, Enhanced performance of single and double junction plastic solar cells, n.d.

[36] J. Gilot, Polymer tandem solar cells, 2010.

[37] J. Gilot, M.M. Wienk, R. a. J. Janssen, Double and triple junction polymer solar cells processed from solution, Applied Physics Letters. 90 (2007) 143512.

[38] M.K. Riede, K.O. Sylvester-Hvid, M. Glatthaar, N. Keegan, T. Ziegler, B. Zimmermann, et al., High throughput testing platform for organic Solar Cells, Progress in Photovoltaics: Research and Applications. 16 (2008) 561-576.

[39] J.D. Servaites, M. a. Ratner, T.J. Marks, Organic solar cells: A new look at traditional models, Energy & Environmental Science. (2011) 4410-4422.

[40] J.H. Lee, S. Cho, A. Roy, H.-T. Jung, A.J. Heeger, Enhanced diode characteristics of organic solar cells using titanium suboxide electron transport layer, Applied Physics Letters. 96 (2010) 163303.

[41] W. Jung, M. Guziewicz, Schottky diode parameters extraction using Lambert W function, Materials Science and Engineering: B. 165 (2009) 57-59.

[42] A. Ortiz-Conde, F.J. Garcia Sanchez, J. Muci, New method to extract the model parameters of solar cells from the explicit analytic solutions of their illuminated characteristics, Solar Energy Materials and Solar Cells. 90 (2006) 352-361.

[43] P. Kumar, S.C. Jain, V. Kumar, S. Chand, R.P. Tandon, A model for the J-V characteristics of P3HT:PCBM solar cells, Journal of Applied Physics. 105 (2009) 104507.

[44] M.-S. Kim, B.-G. Kim, J. Kim, Effective variables to control the fill factor of organic photovoltaic cells., ACS Applied Materials & Interfaces. 1 (2009) 1264-9.

[45] C. Zhang, J. Zhang, Y. Hao, Z. Lin, C. Zhu, A simple and efficient solar cell parameter extraction method from a single current-voltage curve, Journal of Applied Physics. 110 (2011) 064504.

[46] S.R. Valluri, D.J. Jeffrey, R.M. Corless, Some applications of the Lambert <I>W</I> function to physics, Canadian Journal of Physics. 78 (2000) 823-831.

[47] P. Junsangsri, F. Lombardi, Modelling and extracting parameters of organic solar cells, Electronics Letters. 46 (2010) 1462.

[48] A. Petersen, T. Kirchartz, T. Wagner, Charge extraction and photocurrent in organic bulk heterojunction solar cells, Physical Review B. 85 (2012) 1-11.

[49] R.C.I. Mackenzie, T. Kirchartz, G.F.A. Dibb, J. Nelson, Modeling Nongeminate Recombination in P3HT : PCBM Solar Cells, The Journal of Physical Chemistry C. (2011) 9806-9813.

[50] S.R. Cowan, N. Banerji, W.L. Leong, A.J. Heeger, Charge Formation, Recombination, and Sweep-Out Dynamics in Organic Solar Cells, Advanced Functional Materials. (2012) n/a-n/a.

[51] M.C. Scharber, D. Mühlbacher, M. Koppe, P. Denk, C. Waldauf, a. J. Heeger, et al., Design Rules for Donors in Bulk-Heterojunction Solar Cells—Towards 10 % Energy-Conversion Efficiency, Advanced Materials. 18 (2006) 789-794.

[52] M. Kemerink, J.M. Kramer, H.H.P. Gommans, R. a. J. Janssen, Temperature-dependent built-in potential in organic semiconductor devices, Applied Physics Letters. 88 (2006) 192108.

[53] J.G. Simmons, Theory of metallic contacts on high resistivity solids—I. Shallow traps, Journal of Physics and Chemistry of Solids. 32 (1971) 1987-1999.

[54] J. Blakesley, D. Neher, Relationship between energetic disorder and open-circuit voltage in bulk heterojunction organic solar cells, Physical Review B. 84 (2011).

[55] V.D. Mihailetchi, P.W.M. Blom, J.C. Hummelen, M.T. Rispens, Cathode dependence of the open-circuit voltage of polymer:fullerene bulk heterojunction solar cells, Journal of Applied Physics. 94 (2003) 6849.

[56] H. Ishii, K. Sugiyama, E. Ito, K. Seki, Energy Level Alignment and Interfacial Electronic Structures at Organic/Metal and Organic/Organic Interfaces, Advanced Materials. 11 (1999) 605-625.

[57] P. Sehati, S. Braun, L. Lindell, L.M. Andersson, M. Fahlman, Energy-Level Alignment at Metal–Organic and Organic–Organic Interfaces in Bulk-Heterojunction Solar Cells, IEEE Journal of Selected Topics in Quantum Electronics. 16 (2010) 1718-1724.

[58] A. Manor, E. a. Katz, T. Tromholt, F.C. Krebs, Enhancing functionality of ZnO hole blocking layer in organic photovoltaics, Solar Energy Materials and Solar Cells. 98 (2011) 491-493.

[59] L.J. Brillson, Y. Lu, ZnO Schottky barriers and Ohmic contacts, Journal of Applied Physics. 109 (2011) 121301.

[60] P. de Bruyn, D.J.D. Moet, P.W.M. Blom, A facile route to inverted polymer solar cells using a precursor based zinc oxide electron transport layer, Organic Electronics. 11 (2010) 1419-1422.

[61] M.C. Gwinner, Y. Vaynzof, K.K. Banger, P.K.H. Ho, R.H. Friend, H. Sirringhaus, Solution-Processed Zinc Oxide as High-Performance Air-Stable Electron Injector in Organic Ambipolar Light-Emitting Field-Effect Transistors, Advanced Functional Materials. 20 (2010) 3457-3465.

[62] T. Arii, A. Kishi, The effect of humidity on thermal decomposition of zinc acetylacetonate monohydrate, Journal Of Thermal Analysis. 83 (2006) 253-260.

[63] M. Jørgensen, K. Norrman, S. a. Gevorgyan, T. Tromholt, B. Andreasen, F.C. Krebs, Stability of Polymer Solar Cells, Advanced Materials. (2011) n/a-n/a.

[64] J.Y. Kim, S.H. Kim, H.-H. Lee, K. Lee, W. Ma, X. Gong, et al., New Architecture for High-Efficiency Polymer Photovoltaic Cells Using Solution-Based Titanium Oxide as an Optical Spacer, Advanced Materials. 18 (2006) 572-576.

[65] F. Huang, L. Hou, H. Shen, J. Jiang, F. Wang, H. Zhen, et al., Synthesis, photophysics, and electroluminescence of high-efficiency saturated red light-emitting polyfluorene-based polyelectrolytes and their neutral precursors, Journal of Materials Chemistry. 15 (2005) 2499.

[66] L. Wang, B. Liang, F. Huang, J. Peng, Y. Cao, Utilization of water/alcohol-soluble polyelectrolyte as an electron injection layer for fabrication of high-efficiency multilayer saturated red-phosphorescence polymer light-emitting diodes by solution processing, Applied Physics Letters. 89 (2006) 151115.

[67] Z. He, C. Zhong, X. Huang, W.-Y. Wong, H. Wu, L. Chen, et al., Simultaneous enhancement of open-circuit voltage, short-circuit current density, and fill factor in polymer solar cells., Advanced Materials (Deerfield Beach, Fla.). 23 (2011) 4636-43.

[68] F. Huang, H. Wu, Y. Cao, Water/alcohol soluble conjugated polymers as highly efficient electron transporting/injection layer in optoelectronic devices., Chemical Society Reviews. 39 (2010) 2500-21.

[69] J.H. Seo, T.-Q. Nguyen, Electronic properties of conjugated polyelectrolyte thin films., Journal of the American Chemical Society. 130 (2008) 10042-3.

[70] H.-L. Yip, S.K. Hau, N.S. Baek, A.K.-Y. Jen, Self-assembled monolayer modified ZnO/metal bilayer cathodes for polymer/fullerene bulk-heterojunction solar cells, Applied Physics Letters. 92 (2008) 193313.

[71] G. Heimel, L. Romaner, E. Zojer, J.-L. Bredas, The Interface Energetics of Self-Assembled Monolayers on Metals., Accounts of Chemical Research. 41 (2008).

[72] J. Felba, H. Schaefer, Materials and Technology for Conductive Microstructures, in: Nanopackaging, 2008: pp. 239-263.

[73] J. Perelaer, R. Abbel, S. Wünscher, R. Jani, T. van Lammeren, U.S. Schubert, Roll-to-Roll Compatible Sintering of Inkjet Printed Features by Photonic and Microwave Exposure: From Non-Conductive Ink to 40% Bulk Silver Conductivity in Less Than 15 Seconds., Advanced Materials (Deerfield Beach, Fla.). (2012) 1-6.

[74] J.J. Lee, J.C. Park, M.H. Kim, T.S. Chang, S.T. Kim, S.M. Koo, et al., Silver complex inks for ink-jet printing: the synthesis and conversion to a metallic particulate ink, Journal of Ceramic Processing Research. 8 (2007) 219-223.

[75] J. a Carr, K.S. Nalwa, R. Mahadevapuram, Y. Chen, J. Anderegg, S. Chaudhary, Plastic-Syringe Induced Silicone Contamination in Organic Photovoltaic Fabrication: Implications for Small-Volume Additives., ACS Applied Materials & Interfaces. (2012).

[76] C. Pacholski, A. Kornowski, H. Weller, Self-assembly of ZnO: from nanodots to nanorods., Angewandte Chemie (International Ed. in English). 41 (2002) 1188-91.

[77] W.J.E. Beek, M.M. Wienk, M. Kemerink, X. Yang, R. a J. Janssen, Hybrid zinc oxide conjugated polymer bulk heterojunction solar cells., The Journal of Physical Chemistry. B. 109 (2005) 9505-16.

[78] E.B. Gutoff, E.D. Cohen, Coating and Drying Defects, John Wiley & Sons, Inc., Hoboken, NJ, USA, 2006.

[79] E.W. Lam, H. Li, M.A. Schmidt, Silver nanoparticle structures realized by digital surface micromachining, in: TRANSDUCERS 2009 - 2009 International Solid-State Sensors, Actuators and Microsystems Conference, IEEE, 2009: pp. 1698-1701.

[80] D.J. Lee, J.H. Oh, H.S. Bae, Crack formation and substrate effects on electrical resistivity of inkjet-printed Ag lines, Materials Letters. 64 (2010) 1069-1072.

[81] J. Chen, S.J. Bull, Multi-cycling nanoindentation study on thin optical coatings on glass, Journal of Physics D: Applied Physics. 41 (2008) 074009.

[82] C.Y. Jiang, X.W. Sun, K.W. Tan, G.Q. Lo, a. K.K. Kyaw, D.L. Kwong, High-bendability flexible dye-sensitized solar cell with a nanoparticle-modified ZnO-nanowire electrode, Applied Physics Letters. 92 (2008) 143101.

[83] D.M. Tanenbaum, M. Hermenau, E. Voroshazi, M.T. Lloyd, Y. Galagan, B. Zimmermann, et al., The ISOS-3 inter-laboratory collaboration focused on the stability of a variety of organic photovoltaic devices, RSC Advances. (2012) 882-893.

[84] R. Rösch, D.M. Tanenbaum, M. Jørgensen, M. Seeland, M. Bärenklau, M. Hermenau, et al., Investigation of the degradation mechanisms of a variety of organic photovoltaic devices by combination of imaging techniques—the ISOS-3 inter-laboratory collaboration, Energy & Environmental Science. (2012).

[85] T. Young, An Essay on the Cohesion of Fluids, Philosophical Transactions of the Royal Society of London. 95 (1805) 65-87.

[86] dataphysics, Interfacial Chemistry Introduction into Methods of Measuring and Analyzing Contact Angles for the Determination of Surface Free Energies of Solids, in: n.d.

[87] D.Y. Kwok, a. W. Neumann, Contact angle measurement and contact angle interpretation, 1999.

[88] J. Gabel, Surface energy, surface tension and contact angles, (n.d.).

[89] D.K. Owens, R.C. Wendt, Estimation of the Surface Free Energy of Polymers, Journal of Applied Polymer Science. 13 (1969) 1741-1747.

[90] KRÜSS, Wetting Envelope, (n.d.).

[91] B. de Boer, a. Hadipour, M.M. Mandoc, T. van Woudenbergh, P.W.M. Blom, Tuning of Metal Work Functions with Self-Assembled Monolayers, Advanced Materials. 17 (2005) 621-625.